Many-body theory of positronium scattering and pickoff annihilation in noble-gas atoms

A. R. Swann,* D. G. Green,† and G. F. Gribakin‡
School of Mathematics and Physics, Queen's University Belfast, University Road, Belfast BT7 1NN, United Kingdom

(Received 19 July 2022; revised 17 February 2023; accepted 2 March 2023; published 5 April 2023)

The many-body-theory approach to positronium (Ps) interactions with atoms developed by the authors [Phys. Rev. Lett. **120**, 183402 (2018)] is applied to the noble-gas atoms He, Ne, Ar, Kr, and Xe. In this method, the Ps-atom interaction is described by the sum of the electron-atom and positron-atom correlation potentials (self-energies) and the screening of the electron-positron Coulomb interaction by the atomic electrons. Phase shifts and cross sections for elastic scattering are presented, along with values of the pickoff annihilation parameter $^1Z_{\rm eff}$, accounting for short-range electron-positron correlations via vertex enhancement factors. Comparisons are made with available experimental data for elastic and momentum-transfer cross sections and $^1Z_{\rm eff}$. Values of $^1Z_{\rm eff}$ for He and Ne are found to be in near-perfect agreement with experiment; for Ar, Kr, and Xe, they are within 20% of measured values.

DOI: 10.1103/PhysRevA.107.042802

I. INTRODUCTION

Positronium (Ps) is a bound state of an electron and a positron. This is a purely leptonic system and the simplest matter-antimatter compound. Its properties and interactions with matter are of fundamental interest and have applications in many areas [1]. For example, the AEgIS and GBAR experiments at CERN [2–5] aim to test whether gravity affects antimatter equivalently to matter, making antihydrogen in Ps collisions with antiprotons, with Ps produced in a mesoporous material [6]. Ps is widely used in condensed-matter physics to determine pore sizes in nanoporous materials and to probe intermolecular voids in polymers [7]. Ps formation in porous materials is also used to study its interactions with gases, e.g., Xe [8–10], or the interaction between the Ps atoms themselves [11–14], with prospects of room-temperature Bose-Einstein condensation and a γ-ray laser [15–17]. There are also proposals for using a beam of long-lived Rydberg Ps for measuring the free fall of a matter-antimatter system [18] and for detecting positron-atom bound states [19].

The theoretical description of Ps-atom interactions is challenging due to the composite nature of both objects and a significant cancellation between the short-range Ps-atom repulsion (which results from the positron-nucleus repulsion and the Pauli repulsion between the electrons in the target atom and the electron in Ps) and the long-range van der Waals attraction. Accurate calculations must account for virtual excitation of both objects during the collision.

In this work we carry out calculations of Ps scattering by noble-gas atoms at low energies (i.e., below the Ps ionization potential, 6.8 eV). We previously considered this problem in the frozen-target approximation, where virtual excitations of the target atom are neglected, and also using a model van der Waals potential to approximately account for such excitations [20]. The calculated scattering cross sections were in agreement with frozen-target calculations of Blackwood *et al.* [21–23] and stochastic variational calculations [24,25], both frozen-core and with the van der Waals potential. They also broadly agreed with the pseudopotential results of Ref. [26,27]. However, the results did not agree with the experimental data for Ar and Xe, which indicated that the cross sections were very small at low collision energies, suggesting that a Ramsaeur-Townsend minimum may be present [28].

We subsequently developed a many-body theory description of Ps-atom interactions [29], combining the many-body theory description of electron-atom and positron-atom interactions, and including the important effect of screening of the electron-positron Coulomb interaction by the atom. As first applications, we computed scattering cross sections and pickoff annihilation rates $^1Z_{\rm eff}$ for Ps collisions with He and Ne [29]. The cross section for both targets was found to be a rather featureless curve, gently decreasing with increasing collision energy. For He, our results are close to the high-quality coupled-state calculations by Walters *et al.* [30] and confined stochastic variational calculations [31,32]. The calculations of $^1Z_{\rm eff}$ accounted for important short-range electron-positron correlations, which enhance annihilation rates by a factor of two to five over independent-particle-model results [33,34]. For He and Ne, the calculated $^1Z_{\rm eff}$ are within 5%–10% of the values measured at room temperature [35], and for He, within 10% of the $^1Z_{\rm eff}$ from the stochastic variational calculations [31,32].

*a.swann@qub.ac.uk
†d.green@qub.ac.uk
‡g.gribakin@qub.ac.uk

Here we describe the many-body-theory approach in more detail and extend its application to Ar, Kr, and Xe, including a study of the sensitivity of the results to the energies at which the screened Coulomb interaction is calculated. Except where otherwise stated, atomic units (a.u.) are used, with the symbol a_0 denoting the Bohr radius (the atomic unit of length).

II. THEORY

A. Hard-wall confinement

The system under consideration is a ground-state Ps atom moving in the field of a closed-shell many-electron atom. We enclose the entire system in an impenetrable sphere of radius R_c centered on the target atom. This has the effect of making all Ps states discrete [36]. This hard-wall cavity is a key feature of our method. Values of R_c are chosen in such a way that the cavity does not affect the atomic ground state and allows for an accurate description of the distortion of Ps as it interacts with the target atom. This enables us to determine Ps-atom scattering phase shifts from the discrete energy eigenvalues [20].

We construct the Ps wave function as an expansion in the electron and positron states that are solutions of the Dyson equation, which involves the self-energy for the respective particle in the field of the atom. The Ps state satisfies a two-particle Dyson equation (Bethe-Salpeter equation), which we solve to find the expansion coefficients and discrete energy eigenvalues from which the scattering phase shifts can be determined [20]. We now describe each step in detail.

B. Dyson equation for electron or positron

A conventional treatment of an electron or positron interaction with an N-electron atom involves the Schrödinger equation for the total wave function for the $N+1$ particles. In many-body theory we use the Dyson equation (see, e.g., Refs. [37,38]):

$$(H_0 + \Sigma_E)\psi_E = E\psi_E. \tag{1}$$

Here, ψ_E is the single-particle (quasiparticle) wave function of the incident electron or positron, E is its energy, and H_0 is a central-field Hamiltonian that describes the motion of the incident electron or positron in the static field of the atom (including exchange for the electron). The key quantity in Eq. (1) is Σ_E, a nonlocal, energy-dependent correlation potential that is equal to the self-energy part of the single-particle Green's function of the electron or positron in the field of the atom [39]. The self-energy Σ_E acts on ψ_E as an integral operator:

$$\Sigma_E\psi_E = \int \Sigma_E(\mathbf{r},\mathbf{r}')\psi_E(\mathbf{r}')d^3\mathbf{r}'. \tag{2}$$

The self-energy Σ_E is given by an infinite series in powers of the residual electron-electron and/or electron-positron interactions. The terms in this series are conveniently depicted by diagrams. The use of the Hartree-Fock approximation for the atomic electrons and inclusion of the electrostatic (and exchange) interaction in H_0 means that the expansion for Σ_E starts with the second-order diagrams, and the diagrams do not contain elements that describe the electrostatic potential of the atom [40]. For electrons, this also implies the absence from Σ_E of the contribution of the target exchange potential.

As a result of the spherical symmetry of the problem, Eq. (1) can be solved separately for each partial wave of the incident electron or positron. The self-energy is expanded in partial waves as

$$\Sigma_E(\mathbf{r},\mathbf{r}') = \frac{1}{rr'}\sum_{\lambda=0}^{\infty}\Sigma_E^{(\lambda)}(r,r')\sum_{\mu=-\lambda}^{\lambda}Y_{\lambda\mu}(\hat{\mathbf{r}})Y^*_{\lambda\mu}(\hat{\mathbf{r}}'), \tag{3}$$

where $Y_{\lambda\mu}$ is a spherical harmonic. Rather than using the coordinate representation $\Sigma_E(\mathbf{r},\mathbf{r}')$ of the self-energy, it is usually more convenient to work with its matrix elements in the basis of eigenfunctions of H_0, viz.,

$$\begin{aligned}\langle\varepsilon' l'm'|\Sigma_E|\varepsilon lm\rangle &= \iint \varphi^*_{\varepsilon' l'm'}(\mathbf{r}')\Sigma_E(\mathbf{r},\mathbf{r}')\varphi_{\varepsilon lm}(\mathbf{r})d^3\mathbf{r}d^3\mathbf{r}' \\ &= \delta_{ll'}\delta_{mm'}\iint P_{\varepsilon' l'}(r')\Sigma_E^{(l)}(r,r')P_{\varepsilon l}(r)drdr',\end{aligned} \tag{4}$$

where

$$H_0\varphi_{\varepsilon lm}(\mathbf{r}) = \varepsilon\varphi_{\varepsilon lm}(\mathbf{r}), \tag{5}$$

and

$$\varphi_{\varepsilon lm}(\mathbf{r}) = \frac{1}{r}P_{\varepsilon l}(r)Y_{lm}(\hat{\mathbf{r}}). \tag{6}$$

Note that, for brevity, we will often replace the set of quantum numbers εlm by the single label ε.

C. Calculation of the self-energy

Each contribution to $\langle\varepsilon'|\Sigma_E|\varepsilon\rangle$ can be represented by a Goldstone diagram. For the electron, we only include diagrams of the lowest, second order, shown in Fig. 1 (top row). The second-order diagrams are known to provide an accurate description of electron-atom interactions [41–45]. The contribution of the first of these diagrams to $\langle\varepsilon'|\Sigma_E|\varepsilon\rangle$ is

$$\sum_{\substack{\mu,\nu>F\\ n\leqslant F}}\frac{\langle\varepsilon' n|V|\mu\nu\rangle\langle\nu\mu|V|n\varepsilon\rangle}{E+\varepsilon_n-\varepsilon_\mu-\varepsilon_\nu+i\delta}. \tag{7}$$

Here $V = |\mathbf{r}-\mathbf{r}'|^{-1}$ is the electron-electron Coulomb interaction, with matrix elements defined as

$$\langle\nu\mu|V|n\varepsilon\rangle = \iint\frac{\varphi^*_\nu(\mathbf{r}')\varphi^*_\mu(\mathbf{r})\varphi_n(\mathbf{r})\varphi_\varepsilon(\mathbf{r}')}{|\mathbf{r}-\mathbf{r}'|}d^3\mathbf{r}d^3\mathbf{r}', \tag{8}$$

ε_μ is the energy of state μ, etc., δ is a positive infinitesimal. The sum in Eq. (7) runs over the occupied (hole) states n and excited electron states μ and ν, including the positive-energy continuum, F denoting the Fermi level. Due to the presence of the hard sphere, the positive-energy "continuum" states are discrete. This diagram accounts for the main correlation effect in low-energy electron-atom interactions, namely, polarization of the atom. At large distances, it leads to the well-known local polarization potential,

$$\Sigma_E(\mathbf{r},\mathbf{r}') \simeq -\frac{\alpha}{2r^4}\delta(\mathbf{r}-\mathbf{r}'), \tag{9}$$

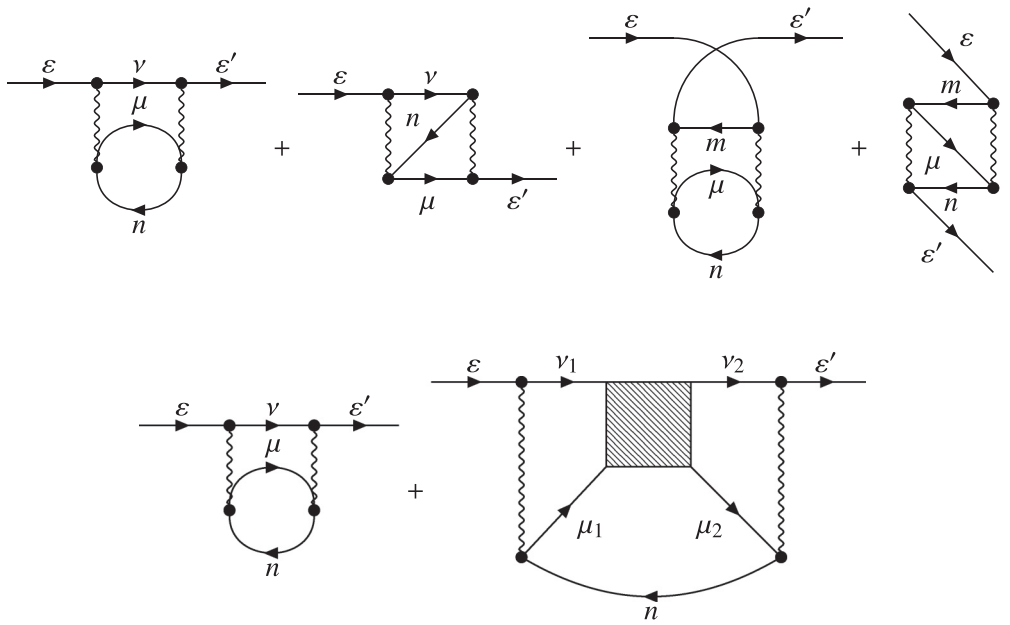

FIG. 1. The main contributions to $\langle\varepsilon'|\Sigma_E|\varepsilon\rangle$ for the electron (top row) and positron (bottom row). Lines labeled ε or ε' represent the electron or positron wave function in the static (Hartree-Fock) field of the atom. Internal lines labeled μ or ν represent either excited electron or positron states, while those labeled m or n represent holes in the atomic ground state. Wavy lines represent electron-electron and electron-positron Coulomb interactions (V and $-V$, respectively). The hatched block (Γ_E) represents the electron-positron ladder-diagram series (see Fig. 2).

where

$$\alpha = \frac{2}{3}\sum_{\substack{\mu>F\\ n\leqslant F}} \frac{|\langle\mu|\mathbf{r}|n\rangle|^2}{\varepsilon_\mu - \varepsilon_n} \tag{10}$$

is the static dipole polarizability of the atom (in the Hartree-Fock approximation here). The other three diagrams are due to electron exchange and ground-state correlations and only contribute to $\langle\varepsilon'|\Sigma_E|\varepsilon\rangle$ at short range.

The main contributions to $\langle\varepsilon'|\Sigma_E|\varepsilon\rangle$ for the positron are shown in Fig. 1 (bottom row). The first diagram produces a long-range polarization potential, similar to that for the electron, cf. Eq. (9). The second diagram describes the important effect of virtual Ps formation [40,46,47]; the hatched block represents the sum of the infinite electron-positron ladder-diagram series Γ_E shown in Fig. 2. This infinite series may be calculated by considering the analytical form of left- and right-hand sides of the diagrammatic equation in Fig. 2,

$$\langle\nu_2\mu_2|\Gamma_E|\mu_1\nu_1\rangle = -\langle\nu_2\mu_2|V|\mu_1\nu_1\rangle - \sum_{\mu',\nu'} \frac{\langle\nu_2\mu_2|\Gamma_E|\mu'\nu'\rangle\langle\nu'\mu'|V|\mu_1\nu_1\rangle}{E - \varepsilon_{\mu'} - \varepsilon_{\nu'} + i\delta}, \tag{11}$$

where $-V$ is the attractive electron-positron Coulomb interaction. Equation (11) is an integral equation for the sum of the ladder diagrams. Due to the hard-sphere confinement [$P_{\varepsilon l}(R_c) = 0$], the electron and positron continua are discretized, and Eq. (11) becomes a linear matrix equation, which can be solved to find the matrix elements of Γ_E [40].

Analytical expressions for each of the diagrams in Fig. 1 are provided in Appendix A.

D. Electron and positron quasiparticle wave functions and energies

In either the electron or positron case, we calculate the self-energy matrix elements $\langle\varepsilon'|\Sigma_E|\varepsilon\rangle$ for pairs of Hartree-Fock states εlm and $\varepsilon' lm$ in the hard-wall cavity. We then solve the Dyson equation (1) to determine the quasiparticle wave functions and energies. To do this, we expand the unknown quasiparticle wave function (also called a *Dyson orbital*) in the basis of Hartree-Fock wave functions,

$$\psi_{Elm}(\mathbf{r}) = \sum_\varepsilon C_\varepsilon \varphi_{\varepsilon lm}(\mathbf{r}). \tag{12}$$

The function $\psi_{Elm}(\mathbf{r})$ can be factorized into radial and angular parts,

$$\psi_{Elm}(\mathbf{r}) = \frac{1}{r}\mathcal{P}_{El}(r)Y_{lm}(\hat{\mathbf{r}}), \tag{13}$$

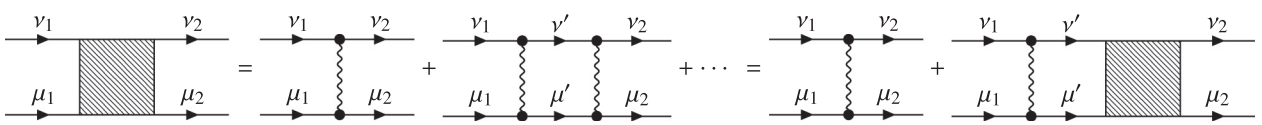

FIG. 2. The electron-positron ladder-diagram series, which accounts for virtual Ps formation. The top line represents the positron, the bottom line is the electron, and the wavy line is their Coulomb interaction $-V$.

with Eq. (12) being an expansion for the radial part:

$$\mathcal{P}_{El}(r) = \sum_{\varepsilon} C_{\varepsilon} P_{\varepsilon l}(r). \tag{14}$$

Substituting Eq. (12) into the Dyson equation (1) and taking matrix elements, we obtain a matrix-eigenvalue equation

$$\mathbf{HC} = E\mathbf{C}, \tag{15}$$

where the Hamiltonian matrix **H** has elements

$$\langle \varepsilon' | H | \varepsilon \rangle = \varepsilon \delta_{\varepsilon\varepsilon'} + \langle \varepsilon' | \Sigma_E | \varepsilon \rangle, \tag{16}$$

and **C** is the vector of expansion coefficients C_ε. Solving Eq. (15) for each partial wave yields the Dyson-orbital energies E and corresponding expansion coefficients for the quasiparticle wave functions. For the electron, the result is a set of negative-energy states corresponding to the atomic orbitals, along with a set of positive-energy "continuum" states. For the positron, all of the states have positive energies.

E. Energy dependence of the self-energy

Because of the dynamic nature of the electron- or positron-atom correlation potential, the self-energy is energy dependent: the energy E appears in the energy denominators of the Goldstone diagrams [see, e.g., Eq. (7)]. However, in finding the Dyson orbitals we do not know the value of E until we have solved Eq. (16), which requires the matrix elements $\langle \varepsilon' | \Sigma_E | \varepsilon \rangle$ to already have been calculated. This means that the Dyson equation must be solved self-consistently, with some initial guess for the energy E being used in $\langle \varepsilon' | \Sigma_E | \varepsilon \rangle$ (e.g., the corresponding Hartree-Fock energy). However, there are two difficulties associated with such an approach.

(1) For any given partial wave of the incident electron or positron, the self-consistent solution of the Dyson equation must be carried out separately for each state, i.e., when solving Eq. (16), only the energy and expansion coefficients for the state under consideration are accurate; the energies and expansion coefficients for the other states must be ignored.

(2) More importantly, if each of the Dyson orbitals is calculated with its own self-energy matrix $\langle \varepsilon' | \Sigma_E | \varepsilon \rangle$ then they will not be mutually orthogonal. Hence, they will not be suitable for constructing the two-particle Ps wave function (see Sec. II F).

In light of this, we have chosen to consistently calculate all of the self-energy diagrams "off the energy shell," at $E = 0$. The energy dependence of the self-energy matrix elements $\langle \varepsilon' | \Sigma_E | \varepsilon \rangle$ is rather weak in the energy range of interest. Using $E = 0$ provides a good description of low-energy electron and positron interactions with noble-gas atoms [29]. In Sec. IV C we briefly investigate the effect of changing the value of E on the results.

F. Two-particle Ps states

Having determined the Dyson-orbital energies and wave functions of the electron and positron states, one can construct a two-particle Ps wave function. The two-particle Dyson equation (also known as the Bethe-Salpeter equation [37]) for Ps moving in the field of the target atom is

$$\left(H_0^e + H_0^p + \Sigma_{E^e}^e + \Sigma_{E^p}^p - V + \delta V_E\right)\Psi = E\Psi, \tag{17}$$

where H_0^e (H_0^p) is the single-particle electron (positron) Hamiltonian [which includes the electron (positron) kinetic energy and the Hartree-Fock potential of the atom], $\Sigma_{E^e}^e$ ($\Sigma_{E^p}^p$) is the self-energy of the electron (positron), $-V$ is the attractive Coulomb interaction between the electron and positron in Ps, and Ψ is the two-particle Ps wave function with energy E.[1] The operator δV_E is the screening correction to the electron-positron Coulomb interaction. The diagrams for the matrix elements $\langle \nu'\mu' | -V + \delta V_E | \mu\nu \rangle$ are shown in Fig. 3; again, we calculate diagrams up to second order. The *direct* screening diagram (the second diagram in Fig. 3) is essential for canceling the long range r^{-4} behavior of the single-particle electron and positron polarization diagrams and making the long-range Ps-atom interaction of the required R^{-6} van der Waals form, where R is the distance between the atomic nucleus and the Ps center of mass. The *exchange* screening diagrams (the third, fourth, and fifth diagrams in Fig. 3) are more expensive to calculate than the direct diagram, but they partially cancel each other and are almost negligible in comparison (see Sec. IV A and Fig. 7); consequently, we will not include the exchange screening diagrams in our calculations. As explained above, the electron and positron self-energies, and the screening correction, are calculated off the energy shell, at $E^e = E^p = E = 0$.

From this point on, we shall, without exception, use the labels μ and ν to refer to electron and positron states in the field of the atom, respectively. The electron and positron Dyson orbitals $\psi_\mu(\mathbf{r}_e)$ and $\psi_\nu(\mathbf{r}_p)$ are eigenstates of the respective single-particle Dyson equation (1). They form orthonormal sets, and we use them to construct a two-particle Ps wave function with a given total angular momentum J and parity Π,

$$\Psi_{J^\Pi}(\mathbf{r}_e, \mathbf{r}_p) = \sum_{\mu,\nu} C_{\mu\nu} \psi_\mu(\mathbf{r}_e)\psi_\nu(\mathbf{r}_p), \tag{18}$$

where the $C_{\mu\nu}$ are expansion coefficients. Since the target atom is closed-shell, the electron part of the Ps wave function should be orthogonal to the occupied atomic orbitals. Hence, the negative-energy electron states corresponding to these atomic orbitals are excluded from Eq. (18). The energy eigenvalues E and expansion coefficients $C_{\mu\nu}$ are found by solving the eigenvalue problem for the Hamiltonian matrix

$$\langle \nu'\mu' | H | \mu\nu \rangle = (\varepsilon_\mu + \varepsilon_\nu)\delta_{\mu\mu'}\delta_{\nu\nu'} + \langle \nu'\mu' | -V + \delta V_E | \mu\nu \rangle, \tag{19}$$

where ε_μ is the energy of state ψ_μ, etc. We consider $J^\Pi = 0^+$, 1^-, and 2^+ to investigate S-, P-, and D-wave Ps scattering, respectively. The Ps energy eigenvalues in the cavity are used to determine the scattering phase shifts, and hence the scattering cross section; see Ref. [20] for details.

[1] There is a similarity between our approach and the combination of MBT with the configuration-interaction method for open-shell atoms [48].

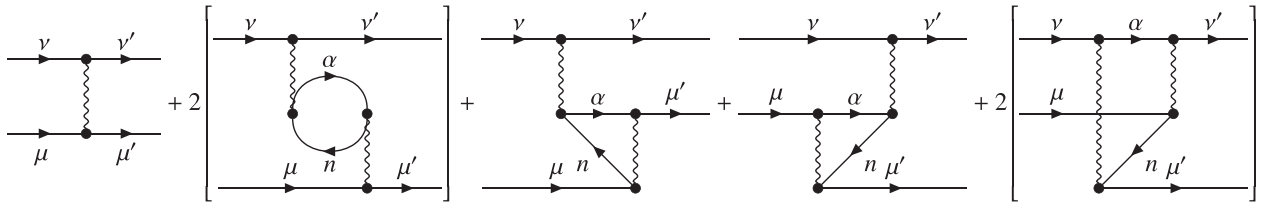

FIG. 3. The main contributions to $\langle\nu'\mu'|-V+\delta V_E|\mu\nu\rangle$. The top line (with end states ν and ν') represents the positron, while the bottom line (with end states μ and μ') represents the electron. The first diagram is the bare Coulomb-interaction matrix element $\langle\nu'\mu'|-V|\mu\nu\rangle$. The second diagram is the *direct* screening diagram; the other diagrams are *exchange* screening corrections. The second and last diagrams are included with factors of two to account for mirror-image diagrams that have identical analytical expressions.

G. Pickoff annihilation

The Ps pickoff annihilation rate λ in a gas is parametrized as

$$\lambda = 4\pi r_0^2 c n {}^1Z_{\rm eff}, \tag{20}$$

where r_0 is the classical electron radius, c is the speed of light, and n is the number density of the gas. The parameter ${}^1Z_{\rm eff}$ (or, more specifically, $4{}^1Z_{\rm eff}$) represents the effective number of atomic electrons available for two-γ-ray pickoff annihilation [49]. In the zeroth-order, independent-particle approximation, ${}^1Z_{\rm eff}$ is given by

$${}^1Z_{\rm eff} = \frac{1}{4}\iiint \rho(\mathbf{r})|\Psi(\mathbf{r}_e,\mathbf{r}_p)|^2\delta(\mathbf{r}-\mathbf{r}_p)d^3\mathbf{r}d^3\mathbf{r}_e d^3\mathbf{r}_p, \tag{21}$$

where $\rho(\mathbf{r}) = \sum_{n\leqslant F}|\psi_n(\mathbf{r})|^2$ is the density of the atomic electrons, and $\Psi(\mathbf{r}_e,\mathbf{r}_p)$ is the Ps wave function, with the Ps center-of-mass motion normalized to a plane wave at large distances. The factor of $\frac{1}{4}$ is to account for the fact that only those electrons that form a relative singlet state with the positron contribute to pickoff annihilation (assuming that all annihilation events are the dominant 2γ decays).

Our interest is in values of ${}^1Z_{\rm eff}$ at small (room-temperature thermal) Ps energies, where the S-wave contribution dominates. Higher partial-wave contributions are suppressed as K^{2L}, where K is the Ps momentum and L is the orbital angular momentum of the Ps center-of-mass motion. We therefore use $\Psi = \Psi_{0^+}$ (with appropriate normalization) in Eq. (21).

To account for the short-range-correlation corrections to ${}^1Z_{\rm eff}$ (neglected in the independent-particle approximation), we augment Eq. (21) with vertex enhancement factors γ_{nl}, which are specific to the electron orbital n and positron partial wave l, and were calculated for positron annihilation in noble-gas atoms in Refs. [33,34]. Explicitly, substituting Eq. (18) into Eq. (21), using orthonormality of the electron wave functions, and introducing the enhancement factors yields

$${}^1Z_{\rm eff} = \frac{1}{4}\sum_{n,\mu,\nu,\nu'}\gamma_{nl}C_{\mu\nu}C^*_{\mu\nu'}\int|\psi_n(\mathbf{r})|^2\psi_\nu(\mathbf{r})\psi^*_{\nu'}(\mathbf{r})d^3\mathbf{r}, \tag{22}$$

where the positron states ψ_ν and $\psi_{\nu'}$ both have angular momentum l (see Appendix A for details of how ${}^1Z_{\rm eff}$ is computed in practice). The enhancement factors are largest for the valence electrons but may still be significant for the core electrons [50]. Also, the values of γ_{nl} are dependent on the energy of the incident positron, although this dependence is not very strong (see Fig. 13 in Ref. [40]). Here we use values of γ_{nl} at zero energy of the positron. Note that γ_{nl} can be calculated using either Hartree-Fock or Dyson states for the positron. Here we use the Hartree-Fock values because, when the positron is "packaged" within Ps, it is shielded from the target atom by its partner electron. The two particles together cannot polarize the atom as much as a lone positron could, and virtual Ps contributes little because the positron already has a partner electron. Table I shows these values of γ_{nl} (taken from Ref. [34]). We leave contributions to ${}^1Z_{\rm eff}$ for core orbitals and/or for $l \geqslant 3$ unscaled, as we find that they generally contribute $\lesssim$1% to ${}^1Z_{\rm eff}$.

III. NUMERICAL IMPLEMENTATION

A. *B*-spline bases

First, a standard Hartree-Fock program [51] is used to compute the electrostatic potential (direct and exchange) of the ground-state target atom. Then, a B-spline basis is used to calculate the single-particle electron and positron Hartree-Fock wave functions $\varphi_{\varepsilon lm}$ (see, e.g., Ref. [40]). We do this for both the electron and positron using two different sets of B splines: the first set contains 40 splines of order six, defined in a cavity of radius $R_c = 30$ a.u., using an exponential knot sequence

TABLE I. Enhancement factors γ_{nl} for atomic orbital n and positron partial wave l [33,34].

Atom	n	$l=0$	$l=1$	$l=2$
He	1s	2.99	4.04	5.26
Ne	1s	1.18	1.21	1.22
	2s	1.87	2.03	2.30
	2p	2.78	3.46	4.70
Ar	2s	1.35	1.38	1.41
	2p	1.43	1.47	1.51
	3s	2.53	2.70	3.00
	3p	5.19	6.22	8.17
Kr	3s	1.34	1.36	1.39
	3p	1.41	1.43	1.47
	3d	1.67	1.72	1.71
	4s	2.77	2.96	3.25
	4p	6.63	7.89	10.33
Xe	4s	1.42	1.44	1.46
	4p	1.52	1.47	1.57
	4d	1.96	2.00	1.24
	5s	3.36	3.59	3.95
	5p	9.26	10.91	14.08

[see Eq. (31) in Ref. [40]]; the second set contains 60 splines of order nine, defined in a cavity of radius $R_c = 10$, 12, 14, or 16 a.u., using a quadratic-linear knot sequence [see Eq. (28) in Ref. [20]]. The reason for using two distinct sets of B splines is as follows: Calculation of the Goldstone diagrams appearing in the expansions of the electron and positron self-energies requires summation over a complete set of intermediate states. The exponential knot sequence is well-suited to this, since it provides rapid saturation of the electron and positron continua (see Fig. 6 in Ref. [40]). However, we ultimately want to use the electron and positron states to construct a two-particle Ps wave function; for this we need the single-particle states to accurately represent "physical" states in the cavity, for which the quadratic-linear knot sequence is well suited [20]. The two sets of Hartree-Fock states for both the electron and positron are used to find the Dyson orbitals in the following manner.

(1) The Hartree-Fock wave functions $\varphi_{\varepsilon lm}$ of the electron or positron, calculated using the exponential knot sequence, are used to compute the self-energy matrix elements $\langle\varepsilon'|\Sigma_E|\varepsilon\rangle$.

(2) These matrix elements are used to find the coordinate form of the self-energy using the completeness relation, viz.,

$$\Sigma_E^{(l)}(r,r') = \sum_{\varepsilon,\varepsilon'} P_{\varepsilon' l}(r')\langle\varepsilon'|\Sigma_E|\varepsilon\rangle P_{\varepsilon l}(r). \tag{23}$$

Here, $P_{\varepsilon' l}(r')$ and $P_{\varepsilon l}(r)$ are the Hartree-Fock radial functions used in step 1, but evaluated at points r and r' on the quadratic-linear knot sequence (see Fig. 2 of Ref. [29] for illustrative plots of $\Sigma^{(l)}(r,r')$ for $l = 0$, 1, 2 for Ne).

(3) The coordinate form of Σ_E is used to calculate its matrix elements via Eq. (4), where now $P_{\varepsilon' l}(r')$ and $P_{\varepsilon l}(r)$ are the Hartree-Fock functions calculated using the *quadratic-linear* knot sequence. (Steps 1–3 are similarly used later for finding the matrix elements of δV_E.)

(4) The Hamiltonian matrix is diagonalized. Its elements are given by Eq. (16), where the matrix elements $\langle\varepsilon'|\Sigma_E|\varepsilon\rangle$ are those calculated in step 3. The eigenvalues are the Dyson-orbital energies of the electron (ε_μ) or positron (ε_ν) in the cavity, and the eigenvectors provide the expansion coefficients for the quasiparticle wave functions in terms of the Hartree-Fock functions on the quadratic-linear knot sequence.

(5) The electron and positron Dyson orbitals are used to construct the Hamiltonian (19) for the Ps states in the cavity.

This method enables the exponential-sequence Hartree-Fock wave functions to be used in the sums over intermediate states of diagrams, thus ensuring good convergence of the sums over the intermediate states, while the Dyson-orbital energies and wave functions are ultimately calculated using the quadratic-linear sequence, meaning that they can be used to accurately describe Ps states in the cavity and determine Ps-atom scattering phase shifts.

Note that, when we construct the two-particle Ps wave function from the single-particle electron and positron states [Eq. (18)], we only use the Dyson-orbital states for the first few partial waves, specifically, $l = 0$–3. To solve the Dyson equation for all angular momenta of the incident electron or positron included in the expansion of the Ps wave function (up to $l = 20$; see Sec. III C) is computationally expensive and unnecessary. For higher l, the centrifugal barrier prevents the electron or positron from approaching the target atom closely, and the effect of correlations (i.e., Σ_E) is small. Hence, we just use the Hartree-Fock states for $l \geqslant 4$.

B. Convergence with respect to number of intermediate states included in diagrams

The use of B splines with exponential knot sequences means that rapid convergence is achieved in the sums over intermediate states in the Goldstone diagrams with respect to the number of radial states included for a particular angular momentum. However, convergence with respect to the number of partial waves included is slower. The increment to the electron or positron eigenenergies upon increasing the maximum orbital angular momentum from $l-1$ to l behaves as $(l+\frac{1}{2})^{-4}$. Therefore, if we include only partial waves up to $l = l_{\max}$, the energy eigenvalues $E(l_{\max})$ approach the ultimate $l_{\max} \to \infty$ values E as follows [52–55]:

$$E(l_{\max}) = E + \frac{A}{\left(l_{\max}+\frac{1}{2}\right)^3}. \tag{24}$$

In practice, we calculate the self-energy diagrams for $l_{\max} = 7$, 8, 9, and 10, diagonalize the Hamiltonian matrix for each value of $l_{\max}$, and extrapolate the resulting eigenenergies using the values for $l_{\max} = 9$ and 10 to find the values of E and A in Eq. (24). We use 32 radial states for each angular momentum in all calculations of second-order diagrams. We find that extrapolation typically changes the $l_{\max} = 10$ value of the energy by less than 0.1%.

When constructing the two-particle Hamiltonian matrix (19) for Ps scattering, we use these extrapolated energies to compute the diagonal elements. The quasiparticle wave functions used in the expansion for the Ps wave function are those obtained for $l_{\max} = 10$.

C. Convergence with respect to number of electron and positron states included in Ps wave function

In Eq. (18), the sums over the electron and positron states should, in theory, run over all orbital angular momenta and radial quantum numbers (up to infinity), but in practice we use finite maximum values $l_{\max}$ and $n_{\max}$, respectively.[2] The resulting dimension $\mathcal{N}$ of the Hamiltonian matrix (19) is

$$\mathcal{N} = \begin{cases} n_{\max}^2(l_{\max}+1) & \text{for} \quad J^\Pi = 0^+ \\ 2n_{\max}^2 l_{\max} & \text{for} \quad J^\Pi = 1^- \\ n_{\max}^2(3l_{\max}-2) & \text{for} \quad J^\Pi = 2^+. \end{cases} \tag{25}$$

To keep the size of the calculations manageable, we used $l_{\max} = n_{\max} = 20$ for $J^\Pi = 0^+$, $l_{\max} = n_{\max} = 18$ for $J^\Pi = 1^-$, and $l_{\max} = n_{\max} = 16$ for $J^\Pi = 2^+$. The Ps eigenenergies are then extrapolated to the limits $l_{\max} \to \infty$ and $n_{\max} \to \infty$ as explained in Ref. [36].

The pickoff annihilation parameter ${}^1Z_{\text{eff}}$ is calculated using Eq. (22) for the lowest-energy state in the cavity. We do this for each cavity radius, $R_c = 10$, 12, 14, 16 a.u., giving values

[2]This $l_{\max}$ is not related to the $l_{\max}$ used in summations over intermediate states in the self-energy diagrams.

of ${}^1Z_{\rm eff}$ for four values of the Ps center-of-mass momentum K. These values are extrapolated in $l_{\rm max}$ according to

$$ {}^1Z_{\rm eff}(l_{\rm max}, n_{\rm max}) = {}^1Z_{\rm eff}(\infty, n_{\rm max}) + \frac{A}{\left(l_{\rm max} + \frac{1}{2}\right)^2}, \tag{26}$$

and subsequently in $n_{\rm max}$ according to

$$ {}^1Z_{\rm eff}(\infty, n_{\rm max}) = {}^1Z_{\rm eff} + \alpha n_{\rm max}^{-\beta}, \tag{27}$$

where we typically find $\beta \approx 4$.

D. Normalization of Ps wave function in calculation of ${}^1Z_{\rm eff}$

In Eq. (22), the Ps wave function needs to be such that the center-of-mass motion is normalized to a plane wave at large distances. However, the wave function of a Ps state in the cavity is normalized as

$$ \iint |\Psi_{0^+}(\mathbf{r}_e, \mathbf{r}_p)|^2 d^3\mathbf{r}_e d^3\mathbf{r}_p = 1. \tag{28}$$

Away from the target atom, the Ps wave function is a product of the internal [Ps($1s$)] and center-of-mass parts [see Eq. (11) in Ref. [20]]. To normalize the center-of-mass motion correctly, we proceed as follows:

(1) The center-of-mass density $\rho_{\rm cm}(\mathbf{r})$ in the cavity is given by

$$ \rho_{\rm cm}(\mathbf{r}) = \iint |\Psi_{0^+}(\mathbf{r}_e, \mathbf{r}_p)|^2 \delta\left(\frac{\mathbf{r}_e + \mathbf{r}_p}{2} - \mathbf{r}\right) d^3\mathbf{r}_e d^3\mathbf{r}_p. \tag{29}$$

The choice $J = 0$ means that $\rho_{\rm cm}(\mathbf{r})$ is spherically symmetric, i.e., it only depends on the distance r of the Ps center of mass from the center of the cavity. We calculate the value of $\rho_{\rm cm}$ on a grid from 0 to R_c, using integer and half-integer values of r. See Appendix A for the details of how $\rho_{\rm cm}(\mathbf{r})$ is computed.

(2) The value of $\rho_{\rm cm}$ for each r is extrapolated to the limit $l_{\rm max} \to \infty$, according to

$$ \rho_{\rm cm}(l_{\rm max}) = \rho_{\rm cm} + \frac{A}{\left(l_{\rm max} + \frac{1}{2}\right)^3}. \tag{30}$$

Extrapolation typically changes the value of $\rho_{\rm cm}$ by 1%–10%, depending on the radius R_c of the cavity. In principle one can also extrapolate in $n_{\rm max}$. However, this changes the value of $\rho_{\rm cm}$ by less than 0.5%, so it has been neglected.

(3) In the asymptotic region of the cavity, i.e., the region where the Ps center of mass is not too close to either the target atom or the cavity wall,[3] the density $\rho_{\rm cm}(\mathbf{r})$ should have the form corresponding to free motion:

$$ \rho_{\rm cm}(\mathbf{r}) = B^2 \frac{\sin^2(Kr + \delta_0)}{(Kr)^2}, \tag{31}$$

where B is a normalization constant, K is the Ps center-of-mass momentum, and δ_0 is the S-wave scattering phase shift. The value of B is determined by performing a least-squares fit of Eq. (31) to the calculated values of $\rho_{\rm cm}$. The phase shift

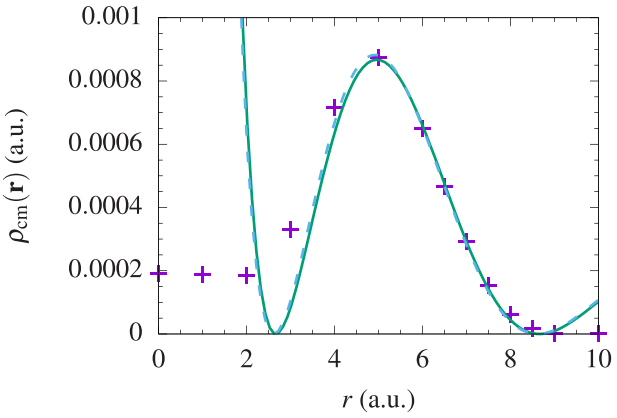

FIG. 4. Center-of-mass density $\rho_{\rm cm}(\mathbf{r})$ for Ps collisions with Ar in a cavity of radius $R_c = 10$ a.u., in the frozen-target approximation. Purple pluses, calculated values of $\rho_{\rm cm}(\mathbf{r})$; solid green line, fit using Eq. (31) with δ_0 as a parameter ($\delta_0 = -1.396$); dashed blue line, fit using Eq. (31) with δ_0 fixed using the boundary condition at the cavity wall ($\delta_0 = -1.374$) [20]. The fits were made by using the calculated values of $\rho_{\rm cm}(\mathbf{r})$ for $5 \leqslant r \leqslant 8.5$ a.u.

δ_0 can be taken from the scattering calculation or allowed to be a free parameter of the fit. Allowing δ_0 to be a variable parameter gives a slightly better fit to the calculated values of $\rho_{\rm cm}$, so we do this in all calculations.[4] Figure 4 shows the center-of-mass density for the lowest-energy Ps eigenstate in collisions with Ar, in a cavity of radius $R_c = 10$ a.u., in the frozen-target approximation [where we excluded Σ_E for both the electron and positron and δV_E from Eq. (17)].

(4) The four values of ${}^1Z_{\rm eff}$ (one for each of $R_c = 10$, 12, 14, 16 a.u.) found directly from Eq. (22) are divided by the corresponding B^2 to obtain correctly normalized values.

Once the four values of ${}^1Z_{\rm eff}$ have been calculated and normalized, the general dependence of ${}^1Z_{\rm eff}$ on the Ps momentum K is analyzed using the effective-range-theory fit

$$ {}^1Z_{\rm eff}(K) = {}^1Z_{\rm eff}(0) + {}^1Z'_{\rm eff} K^2, \tag{32}$$

where ${}^1Z_{\rm eff}(0)$ and ${}^1Z'_{\rm eff}$ are parameters to be determined [56].

IV. RESULTS

We have previously reported the scattering cross sections and values of ${}^1Z_{\rm eff}$ for He and Ne in Ref. [29]; however, we include them again here for ease of comparison with the current results for Ar, Kr, and Xe.

[3]The asymptotic region is roughly defined by $r_{\rm at} \ll r < R_c - \rho_{1s}$, where $r_{\rm at}$ is the approximate radius of the target atom, and ρ_{1s} is the collisional radius of Ps with respect to the cavity wall [36].

[4]Alternatively, one can estimate the value of B^2 analytically by modeling the target atom as a hard sphere of radius $r_{\rm at}$. Assuming $\rho_{\rm cm}(\mathbf{r}) = B^2 \sin^2(Kr + \delta_0)/(Kr)^2$ for $r_{\rm at} < r < R_c$, and using the fact that $\rho_{\rm cm}$ is normalized to unity in the cavity, we obtain $(4\pi B^2/K^2) \int_{r_{\rm at}}^{R_c - \rho_{1s}} \sin^2(Kr + \delta_0) dr = 1$, where ρ_{1s} is the collisional radius of ground-state Ps. Since $r_{\rm at} < r < R_c$ corresponds to a half period of $\sin(Kr + \delta_0)$, i.e., $K(R_c - \rho_{1s} - r_{\rm at}) = \pi$, we have $\int_{r_{\rm at}}^{R_c - \rho_{1s}} \sin^2(Kr + \delta_0) dr = \pi/2K$, and therefore $B^2 = K^3/2\pi^2$.

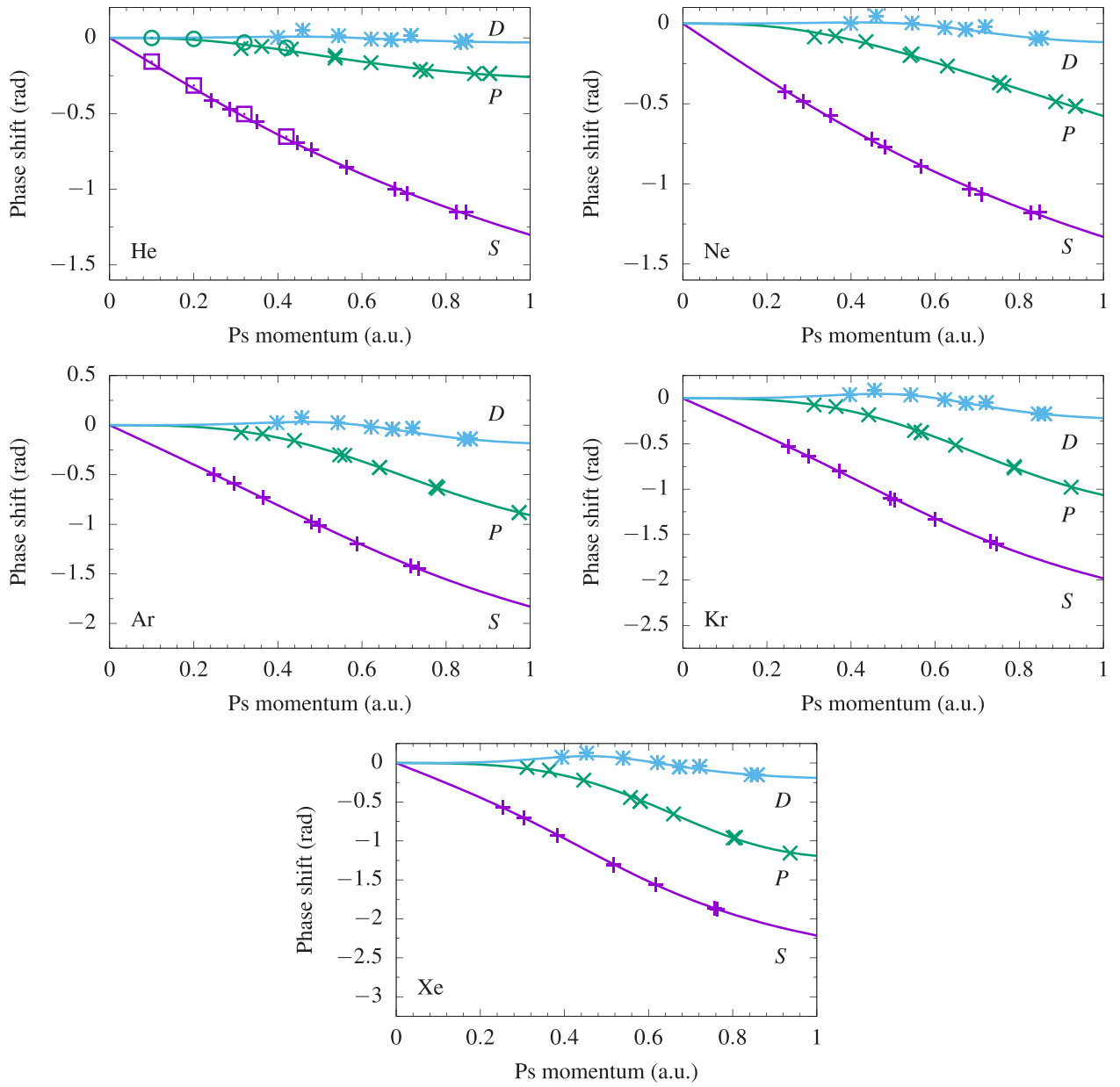

FIG. 5. *S*-, *P*-, and *D*-wave scattering phase shifts obtained for Ps scattering on He, Ne, Ar, Kr, and Xe. Purple pluses, calculated δ_0; green crosses, calculated δ_1; blue asterisks, calculated δ_2; solid purple lines, effective-range fits for δ_0; solid green lines, effective-range fits for δ_1; solid blue lines, effective-range fits for δ_2 (see Appendix B). For He we also show results (*S* and *P* waves only) from the confined stochastic variational calculation: purple squares, δ_0; green circles, δ_1 [31,32].

A. Scattering

Figure 5 shows the *S*-, *P*-, and *D*-wave scattering phase shifts δ_L obtained for Ps collisions with He, Ne, Ar, Kr, and Xe. The phase shifts are calculated at discrete values of the Ps center-of-mass momentum K, with effective-range-theory fits used to describe the general dependence of δ_L on K; see Appendix B for details. In spite of the large differences in the sizes and polarizabilities of the atoms, there is a great degree of similarity between the phase shifts for all of them. This is a result of cancellation of the effect of increasing repulsion in the He to Xe sequence (due to increasing atomic sizes) and increasing strength of the correlation (van der Waals–type) attraction between the Ps and the atom. Note that the *S*-wave phase shift is negative at low K for all five target atoms, i.e., the scattering length is positive for all of them. Therefore, we can immediately deduce that a Ramsauer-Townsend minimum will not appear in any of our cross sections, in contrast with the experimental prediction [28]. Note also that for He, our results are in a good agreement with the *S*- and *P*-wave phase shifts obtained in the confined stochastic-variational calculations [31,32].

Table II lists the present scattering lengths and zero-energy cross sections, alongside data from a number of earlier calculations: the frozen-target calculations and model van der Waals calculations of Swann and Gribakin [20]; the coupled-channel *R*-matrix calculation for He (which included nine Ps states and nine He states in the channel space) [30]; quantum

TABLE II. Scattering lengths A (in units of a_0) and zero-energy cross sections $\sigma(0)$ (in units of πa_0^2) for Ps scattering on He, Ne, Ar, Kr, and Xe.

Method	A	$\sigma(0)$
Ps-He calculations and experiment		
Present, many-body theory	1.70	11.6
Frozen target [20]	1.86	13.8
van der Waals, $R_0 = 2.5$ a.u. [20]	1.52	9.2
van der Waals, $R_0 = 3.0$ a.u. [20]	1.61	10.4
Quantum Monte Carlo [57]	1.405	7.90
R matrix, 9 Ps states, 9 He states [30]	1.6	9.9
Stochastic variational (with stabilization) [31]	1.57	9.9
Experiment	1.46 ± 0.08 [58]	
	1.51 ± 0.18 [59]	
	1.49 [60]	
	1.42 [61]	
	1.50 [62]	
	1.77 ± 0.25 [63]	
	$1.18^{+0.3}_{-0.4}$ [64]	
Ps-Ne calculations		
Present, many-body theory	1.76	12.4
Frozen target [20]	2.02	16.4
van der Waals, $R_0 = 2.5$ a.u. [20]	1.46	8.5
van der Waals, $R_0 = 3.0$ a.u. [20]	1.66	11.0
Stochastic variational, van der Waals [24]	1.55	9.6
Ps-Ar calculations		
Present, many-body theory	1.98	15.6
Frozen target [20]	2.81	31.6
van der Waals, $R_0 = 2.5$ a.u. [20]	1.43	8.2
van der Waals, $R_0 = 3.0$ a.u. [20]	2.16	18.7
Stochastic variational, van der Waals [24]	1.79	12.8
Pseudopotential, van der Waals [26]	2.14	18.3
Ps-Kr calculations		
Present, many-body theory	2.06	17.0
Frozen target [20]	3.11	38.7
van der Waals, $R_0 = 3.0$ a.u. [20]	2.26	20.4
van der Waals, $R_0 = 3.5$ a.u. [20]	2.56	26.2
Stochastic variational, van der Waals [25]	1.98	15.6
Pseudopotential, van der Waals [26]	2.35	22.1
Ps-Xe calculations		
Present, many-body theory	2.12	18.1
Frozen target [20]	3.65	53.3
van der Waals, $R_0 = 3.0$ a.u. [20]	2.63	27.7
van der Waals, $R_0 = 3.5$ a.u. [20]	2.88	33.2
Stochastic variational, van der Waals [25]	2.29	20.9
Pseudopotential, van der Waals [27]	2.45	24.0

Monte Carlo calculations for He [57]; stochastic variational calculations for He [31]; fixed-core stochastic-variational calculations for Ne, Ar, Kr, and Xe (which included model one-body and two-body polarization potentials for the electron and positron) [24,25]; and the calculations of Fabrikant and coworkers where the electron- and positron-atom interactions were modeled using pseudopotentials, with a model van der Waals potential [26,27].

For Ps scattering on He, we obtain a scattering length of 1.70 a.u., which is close to our previous calculation [20] that employed a model van der Waals potential (with $R_0 = 3.0$ a.u.; see Eq. (24) in Ref. [20]), the 9-Ps–9-He–state R-matrix calculation of Walters *et al.* [30], and the stochastic-variational calculation of Zhang and Mitroy [31] (at the level of 6%–8%). Comparing with experiment, it is closest to, and within the error bars of, the value of Nagashima *et al.* [63], with most other measurements giving slightly smaller values. Our scattering length corresponds to a zero-energy cross section of $11.6\pi a_0^2$. Note that correlation effects reduce the scattering length from its frozen-target value [20] by 9%, and the zero-energy cross section by 16%.

The scattering lengths for Ne, Ar, Kr, and Xe are 1.76, 1.98, 2.06, and 2.12 a.u., respectively. The reduction of the scattering length from its frozen-target value [20] increases with the atomic number of the target, from 13% for Ne to 41% for Xe. Indeed, the zero-energy cross section for Xe is approximately one third of its frozen-target value. These results show that the van der Waals interaction due to simultaneous distortion of the Ps and the target plays a significant role in Ps-atom scattering and must be accounted for in order to obtain accurate results. Its effect is greater for heavier, more polarizable atoms. Compared with other predictions, our calculations are closest to the stochastic-variational results of Mitroy and coworkers [24,25] which account for the van der Waals interaction through model one- and two-body polarization potentials.

Figure 6 shows the elastic scattering cross sections as functions of the Ps center-of-mass momentum K, up to $K = 1$ a.u. (the Ps breakup threshold). They are generally rather flat and featureless, and come into good agreement with the previous van der Waals calculations [20] at higher Ps momenta. The cross section for He is also within ≈10% of the 9-Ps–9-He–state calculation of Walters *et al.* [30], and the confined stochastic variational calculation of Wu *et al.* [32].

As we move along the noble-gas atom sequence, the behavior of the cross section at low energy changes from being decreasing for He, Ne, and Ar to almost flat for Kr, and to gently increasing for Xe. This is caused by the increasing P-wave contribution at intermediate momenta. This increase is due to a larger static Ps-atom repulsion for the heavier noble-gas atoms, which overcomes the stronger dispersion interaction for these more polarisable atoms. The contribution of the D wave remains small for all atoms.

The level of agreement with the experimental data available for Ar and Xe [28] is mixed. For Xe there is close agreement for $0.6 \lesssim K \lesssim 0.8$ a.u. However, the measured cross section for $K = 0.44$ a.u. is about a factor of two lower than our theoretical prediction, and the two measured values with the highest momenta indicate an increase in the cross section, in contrast to our calculation. For Ar, the cross sections agree at $K = 0.8$ a.u. The Ps $n = 2$ excitation threshold lies at $K = \sqrt{3}/2 \approx 0.87$ a.u., so it is possible that for $K > 0.87$ a.u. inelastic scattering with excitation of Ps($n = 2$) states, which is neglected in our calculations, contributes to the measured values.

Curiously, for Ar, Kr, and especially Xe, our cross sections begin to decrease markedly at $K \approx 0.8$ a.u. Behavior of this type was not seen in either the frozen-target or van der Waals calculations (although the frozen-target and van der Waals cross sections were much more strongly decreasing

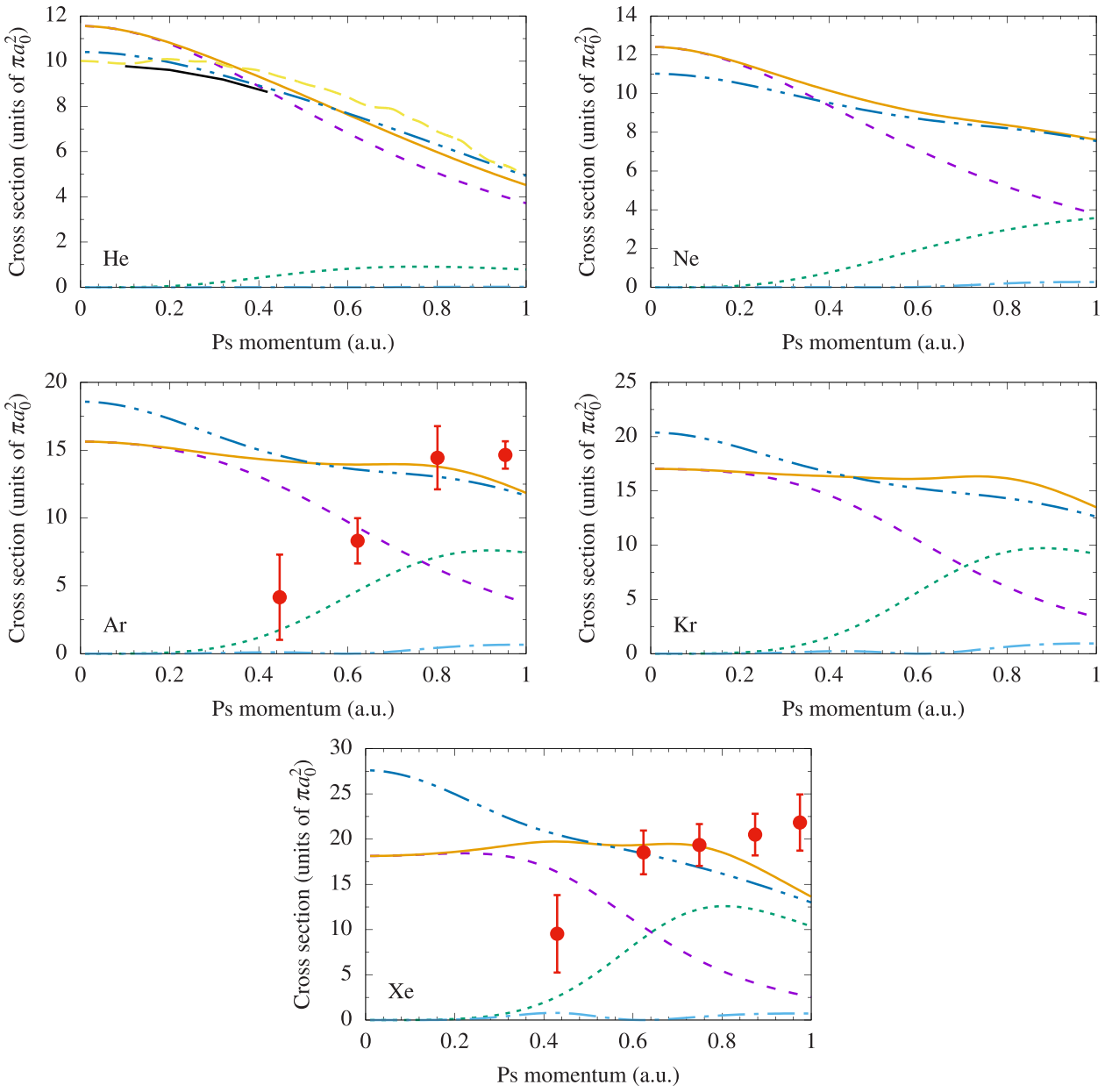

FIG. 6. Elastic scattering cross sections for Ps scattering on He, Ne, Ar, Kr, and Xe. Present calculations: dashed purple lines, S-wave partial cross section; dotted green lines, P-wave partial cross section; dot-dashed light blue lines, D-wave partial cross section; solid orange lines, total cross section. Additional calculations of total cross section: dot-dash-dotted dark blue lines, van der Waals calculations with $R_0 = 3.0$ a.u. [20]. For He: long-dashed yellow line, 9-Ps–9-He coupled-channel calculation [30]; solid black line, stochastic variational calculation with S- and P-wave contributions only [32]. The red circles are the experimental measurements of the total cross section by Brawley *et al.* [28].

across all momenta) [20]. It appears to occur because the P-wave partial cross section reaches its maximum and begins to decrease at $K \approx 0.8$–0.9 a.u., while the D-wave partial cross section remains almost insignificantly small—much smaller than in the frozen-target or van der Waals calculations [20] (due to cancellation of the static repulsion and correlation attraction). It is, however, possible that our calculations become less accurate at momenta $K > 0.8$ a.u., where the Ps energy is close to the Ps($n = 2$) excitation threshold.

The effect of including or excluding the exchange screening diagrams (see Fig. 3) on the scattering cross section has been investigated for Ar. Figure 7 shows the total cross section for Ar in three different approximations: including only the direct screening diagram in δV, including the direct and exchange diagrams in δV, and completely neglecting the screening correction δV (i.e., treating the interaction between the electron and positron as just the bare Coulomb interaction). Also shown is the previous van der Waals calculation with $R_0 = 3.0$ a.u. [20]. It is evident that including only the direct screening diagram or including the direct and exchange screening diagrams in δV gives very similar cross sections, differing by no more than 2% across the momentum range considered. It is therefore justified, at this level of accuracy, to neglect the exchange screening diagrams, saving computational expense required to calculate them. Note that these cross sections have the same basic shape as the earlier

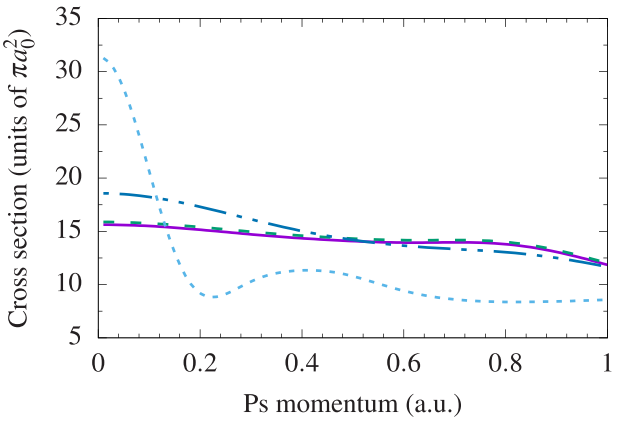

FIG. 7. Cross section for Ps scattering on Ar in various approximations. Solid purple line, inclusion of direct screening diagram only; dashed green line, inclusion of direct and exchange screening diagrams; dotted light blue line, neglecting the screening correction. The dot-dash-dotted dark blue line is the previous van der Waals calculation with $R_0 = 3.0$ a.u. [20].

van der Waals cross section [20], coming into very close agreement for $K \gtrsim 0.5$ a.u. In fact, it is quite remarkable that using a simple, local van der Waals potential with a single fitting parameter gives the cross section in such close agreement with the sophisticated *ab initio* many-body-theory calculation. One may conclude from this that this potential (with a judiciously chosen cutoff radius) captures well the correlation effects in the Ps-atom interaction.

The calculation which neglects the screening correction δV (dotted line in Fig. 7) displays a much more vigorous energy dependence, and is in stark contrast with the others. As mentioned in Sec. II F, the screening correction δV (which is physically similar to the two-body polarization potential [24]) cancels the long-range $-\alpha/2r^4$ polarization potentials acting on the electron and positron, resulting in the correct $-C_6/R^6$ asymptotic behavior of the Ps-atom interaction. Neglecting δV thus leads to a severe overestimation of the Ps-atom correlation attraction and larger S- and P-wave phase shifts. The corresponding S-wave cross section displays a Ramsauer-Townsend minimum, leading to the cross section seen in Fig. 7.

Figure 8 shows the momentum-transfer cross sections for He, Ne, Ar, Kr, and Xe, along with the corresponding van der Waals calculations using $R_0 = 3.0$ a.u. [20]. For comparison, the elastic cross sections are also shown. Moving away from $K = 0$, the momentum-transfer cross sections all drop below the corresponding elastic cross sections rather rapidly (due to destructive interference of the S- and P-wave contributions), and the many-body-theory and van der Waals calculations coalesce at high K. Also shown in Fig. 8 are the experimental data from several groups, which are not direct measurements but the results extracted from observation of Ps thermalization in the noble gases.

For He, our calculation lies within the error bars of the experimental result of Nagashima *et al.* [63] but is about 30%–45% higher than the earlier measurements of Canter *et al.* [58], Rytsola *et al.* [61], and Coleman *et al.* [62]. The measurements of Skalsey *et al.* [65] and Engbrecht *et al.* [64] give much lower values, and the zero-energy cross section according to Engbrecht *et al.* [64] is not consistent with the measurements of Canter *et al.* [58], Rytsola *et al.* [61], and Coleman *et al.* [62]. As we noted in Ref. [29], this may be because the measurements of Skalsey *et al.* [65] and Engbrecht *et al.* [64] are based on Doppler-broadening spectroscopy, and they may suffer from errors related to the discrimination of the narrow Ps annihilation component on the background of the positron-He annihilation signal.

For Ne, our calculation is in agreement with the results of Skalsey *et al.* [65], but lies outside the error bars of the measurement of Saito *et al.* [66], and is about 40% greater than the result of Coleman *et al.* [62]. For Ar, there is agreement with the measurement by Nagashima *et al.* [67], but the discrepancy with the results of Coleman *et al.* [62], Skalsey *et al.* [65], and Sano *et al.* [68] is at the level of 70%, 60%, and 300%, respectively. The general trend of the experimental data for Ar is a rapid decrease of the momentum-transfer cross section with increasing energy, which is qualitatively similar to our results but faster than the calculation predicts. Finally, for Xe, our momentum-transfer cross section is approximately 30% greater than the experimental value of Shibuya *et al.* [9] at Ps energies of 40–60 meV, obtained by studying the time evolution of the annihilation signal during Ps thermalization in Xe. A more advanced partial-wave analysis by the same group [10] yields the zero-momentum cross section of $(15 \pm 2) \times 10^{-16}$ cm^2, which is in agreement with the present calculation.

B. Pickoff annihilation

Table III shows the values of ${}^1Z_{\rm eff}(0)$ and ${}^1Z'_{\rm eff}$ obtained by fitting the calculated ${}^1Z_{\rm eff}$ [see Eq. (32)], and provides a comparison with existing calculations and experimental data. The experimental values of ${}^1Z_{\rm eff}$ usually refer to room-temperature, thermalized Ps, with $K \approx 0.06$ a.u., but can be compared with ${}^1Z_{\rm eff}(0)$, given the weak momentum dependence of ${}^1Z_{\rm eff}(K)$.

We carried out three sets of calculations for each target atom: frozen-target calculations, where we excluded Σ_E for both the electron and positron and δV_E from Eq. (17) and set $\gamma_{nl} = 1$ for all atomic orbitals and positron angular momenta in Eq. (22); *unenhanced* many-body-theory calculations, where we included Σ_E for both the electron and positron and δV_E in Eq. (17) but kept $\gamma_{nl} = 1$ for all atomic orbitals and positron angular momenta in Eq. (22), and *enhanced* many-body-theory calculations, where we included Σ_E for both the electron and positron and δV_E in Eq. (17) and use the values of γ_{nl} given in Table I in Eq. (22). In addition to the above many-body-theory results obtained with $E = 0$ (see Sec. II E), Table III also shows ${}^1Z_{\rm eff}(0)$ and ${}^1Z'_{\rm eff}$ obtained using the more physical value $E = -0.375$ a.u. We regard the latter results as our recommended values and discuss them separately in Sec. IV C.

For He, where several static-exchange calculations of ${}^1Z_{\rm eff}(0)$ are available, the present frozen-target results differ from those of Refs. [69,70,72,73] by 17%, 21%, 35%, and 75%, respectively. A difference of about 20% is not unexpected, because unlike the present frozen-target calculations, the static-exchange calculations do not account for distortion

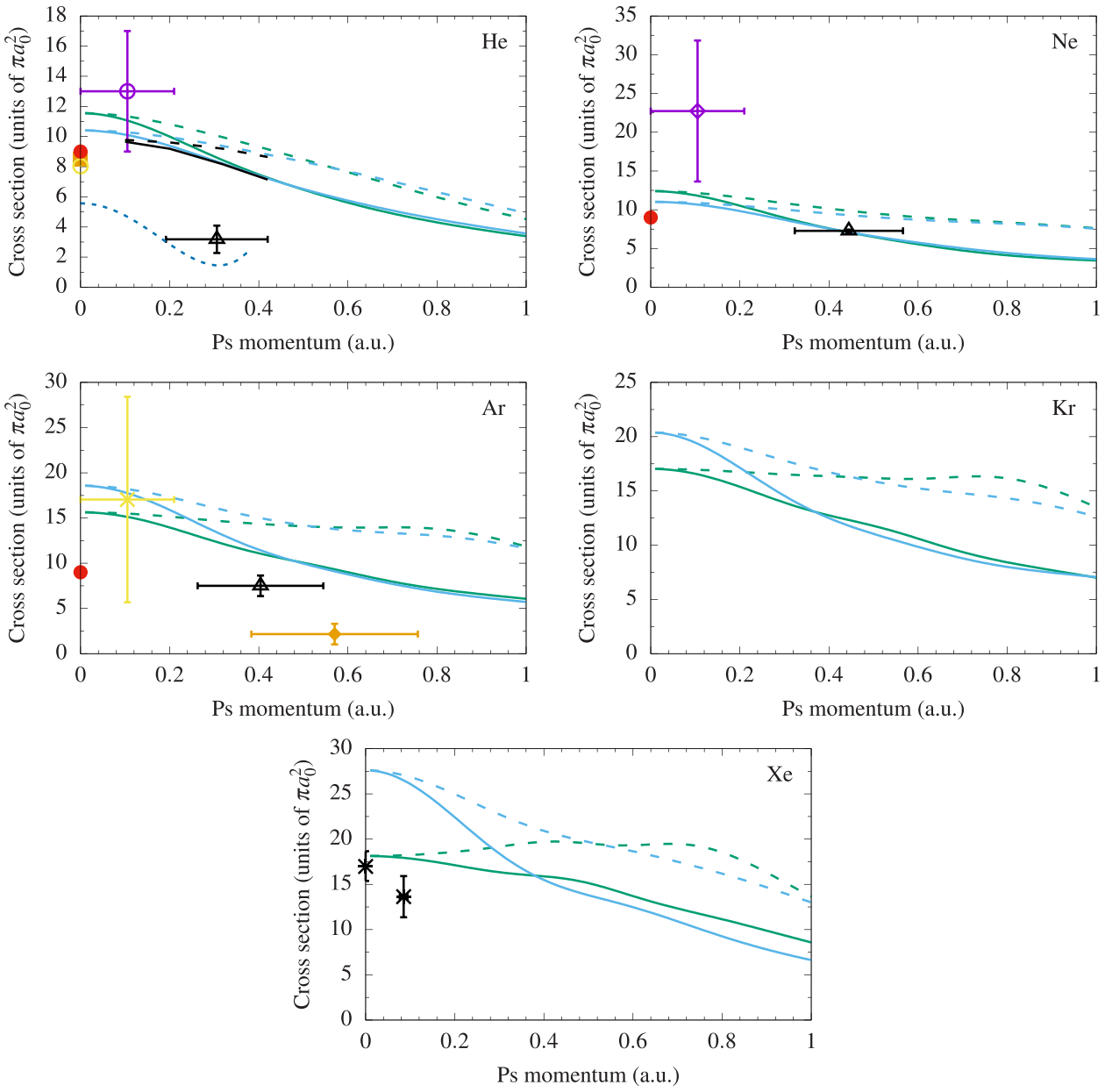

FIG. 8. Momentum-transfer and total elastic cross sections for Ps scattering on He, Ne, Ar, Kr, and Xe. Solid (dashed) green lines, momentum-transfer (elastic) cross section using many-body theory; solid (dashed) light blue lines, momentum-transfer (elastic) cross section using model van der Waals potential with $R_0 = 3.0$ a.u. Also shown for He as a solid (dashed) black line is the confined stochastic variational calculation (S and P waves only) [32]. Measurements of momentum-transfer cross section: filled orange square, Canter *et al.* [58]; open yellow circle, Rytsola *et al.* [61]; filled red circle, Coleman *et al.* [62]; open black triangle, Skalsey *et al.* [65]; open purple circle, Nagashima *et al.* [63]; dotted dark blue line, Engbrecht *et al.* [64]; open purple diamond, Saito *et al.* [66]; yellow cross, Nagashima *et al.* [67]; filled orange diamond, Sano *et al.* [68]; black asterisks, Shibuya *et al.* [9,10].

of the Ps projectile. As for the much larger discrepancies with Refs. [72,73], it was pointed out earlier by Mitroy and Ivanov [24] that the model exchange interaction used in Ref. [73] was of "dubious validity," and the fact that the value of $^1Z_{\rm eff}(0)$ in Ref. [73] is in excellent agreement with experiment [35] is a coincidence. In fact, this static-exchange calculation is in poor agreement with the other static-exchange calculations [69,70]), and one of the authors of Ref. [72] later stated that an assumption made therein (that the direct potential is negligible compared with the exchange potential) was not quantitatively correct [75].

Unlike the experimental data, which show an increase in $^1Z_{\rm eff}$ along the noble-gas-atom sequence, our frozen-target value of $^1Z_{\rm eff}(0)$ increases between He and Ne, but decrease from Ne through to Xe. The frozen-target stochastic variational calculations of Mitroy and coworkers [24,25] are within a few percent of our data, and also increase from He to Ne, and then steadily decrease. These trends indicate that distortion of the target atom and short-range electron-positron correlations are much more important for explaining the observed $^1Z_{\rm eff}$ in heavier target atoms. Compared with the experimental data [35,74], the frozen-target values of $^1Z_{\rm eff}(0)$ are an order of

TABLE III. Pickoff annihilation parameters $^1Z_{\rm eff}(0)$ and $^1Z'_{\rm eff}$ for Ps collisions with noble-gas atoms. The abbreviation VE means "vertex enhancement." We quote results for the many-body theory with energy denominators calculated with $E = 0$ and the more physical $E = -0.375$ a.u. (denoted "$E < 0$" below), with the latter (in bold) representing our best results (see discussion on energy E dependence of diagrams in Sec. IV C and Table IV below).

Method	$^1Z_{\rm eff}(0)$	$^1Z'_{\rm eff}$
Ps-He collisions		
Present, frozen target	0.0273	0.0101
Present, many-body theory without VE, $E = 0$	0.0411	0.00281
Present, many-body theory with VE, $E = 0$	0.131	0.00809
Present, many-body theory with VE, $E < 0$	**0.124**	
Static exchange (not converged) [49]	0.0177	
Static exchange [69]	0.033	
Static exchange [70]	0.0347	
Static exchange with van der Waals [71]	0.0445	
Kohn variational, static exchange [72]	0.042	
T matrix, model static exchange [73]	≈0.11	≈1.4
Stochastic variational, frozen target [24]	0.0287	0.0044
Stochastic variational, van der Waals [24]	0.0378	−0.0152
Stochastic variational, with stabilization [31]	0.1157	
Confined variational [32]	0.1197	
Experiment [35]	0.125	
Ps-Ne collisions		
Present, frozen target	0.0512	0.0170
Present, many-body theory without VE, $E = 0$	0.0932	−0.00482
Present, many-body theory with VE, $E = 0$	0.255	−0.0315
Present, many-body theory with VE, $E < 0$	**0.231**	
Stochastic variational, frozen target [24]	0.0533	0.0100
Stochastic variational, van der Waals [24]	0.0922	−0.0717
Experiment [35]	0.235	
Ps-Ar collisions		
Present, frozen target	0.0316	0.0253
Present, many-body theory without VE, $E = 0$	0.103	−0.0836
Present, many-body theory with VE, $E = 0$	0.516	−0.448
Present, many-body theory with VE, $E < 0$	**0.375**	
Stochastic variational, frozen target [24]	0.0340	0.0084
Stochastic variational, van der Waals [24]	0.0964	−0.168
Experiment [35]	0.314	
Ps-Kr collisions		
Present, frozen target	0.0304	0.00687
Present, many-body theory without VE, $E = 0$	0.109	−0.111
Present, many-body theory with VE, $E = 0$	0.678	−0.731
Present, many-body theory with VE, $E < 0$	**0.446**	
Stochastic variational, frozen target [25]	0.0300	0.0247
Stochastic variational, van der Waals [25]	0.0913	−0.211
Experiment [74]	0.36	
Ps-Xe collisions		
Present, frozen target	0.0261	0.00693
Present, many-body theory without VE, $E = 0$	0.114	−0.151
Present, many-body theory with VE, $E = 0$	0.939	−1.24
Present, many-body theory with VE, $E < 0$	**0.530**	
Stochastic variational, frozen target [25]	0.0223	0.0165
Stochastic variational, van der Waals [25]	0.0891	−0.318
Experiment [74]	0.48	

magnitude too small, which is not surprising, given the neglect of the correlation effects.

Our many-body-theory calculations of $^1Z_{\rm eff}(0)$, without account of annihilation vertex enhancement, are larger than the frozen-target values by a factor that ranges from 1.5 (for He) to 4.4 (for Xe). These increased values of $^1Z_{\rm eff}(0)$ are within ≈20% of the stochastic variational results of Mitroy and coworkers [24,25] with a model-potential inclusion of the van der Waals interaction. However, they still underestimate the experimental data [35,74] by a factor of 2–4 as a result of the missing short-range electron-positron correlation effects.

Including the vertex enhancement factors in Eq. (22) results in an order-of-magnitude increase in $^1Z_{\rm eff}(0)$ from the frozen-target value for all of the atoms. For He and Ne, there is now close agreement with experiment [35], at the level of 5% and 9%, respectively. In both cases, our calculation slightly overestimates the experiment. The result for He is also within ≈10% of the results of the confined stochastic variational calculations [31,32], which include electron-positron correlation effects in the explicitly correlated Gaussian wave function.

For Ar, Kr, and Xe, our many-body calculations of $^1Z_{\rm eff}(0)$ overestimate the experiment [35,74] by factors of 1.6, 1.9, and 2.0, respectively. The value of $^1Z'_{\rm eff}$ has changed sign from positive (in the frozen-target approximation) to negative for Ne, Ar, Kr, and Xe. For Ar, Kr and Xe, these values also become noticeably larger in magnitude, compared with the frozen-core results, indicating a stronger momentum dependence of $^1Z_{\rm eff}$. Note that these changes occur when the many-body-theory Ps wave function is used to calculate $^1Z_{\rm eff}$, even when the enhancement of the annihilation vertex is neglected (see Table III). This suggests that this effect is due to the correlated (van der Waals-type) Ps-atom interaction, which becomes particularly strong for the heavier noble-gas atoms. A possible explanation for this phenomenon is as follows: In the frozen-target approximation, the overall Ps-atom interaction is repulsive. With increasing energy, the Ps overcomes this repulsion to some extent and penetrates the target atom more, making pickoff annihilation more likely; hence $^1Z'_{\rm eff} > 0$. When the Dyson-orbital states and screening corrections are used to construct the Ps wave function, the dispersion interaction affects the Ps mostly at low energy; hence $^1Z_{\rm eff}(0)$ increases significantly. At higher energy the effect of electron- and positron-atom correlations decreases, and values of $^1Z_{\rm eff}$ get closer to what they were in the frozen-target approximation; hence $^1Z'_{\rm eff}$ reduces (and happens to become negative for Ne, Ar, and Kr).

Our vertex-enhanced many-body-theory values of $^1Z_{\rm eff}(0)$ increase monotonically with the atomic number, as observed in experiment [35,74]. However, our theoretical approach appears to systematically overestimate the measured $^1Z_{\rm eff}$, and the discrepancy increases for heavier, more polarizable targets. Possible explanations for this behavior are as follows:

(1) The Ps may be too strongly attracted to the target atom, i.e., the correlation potential for the electron and/or positron may be too attractive. There is a possibility that the electron and positron self-energy and the screening correction should all be smaller due to the fact that the energy E that appears

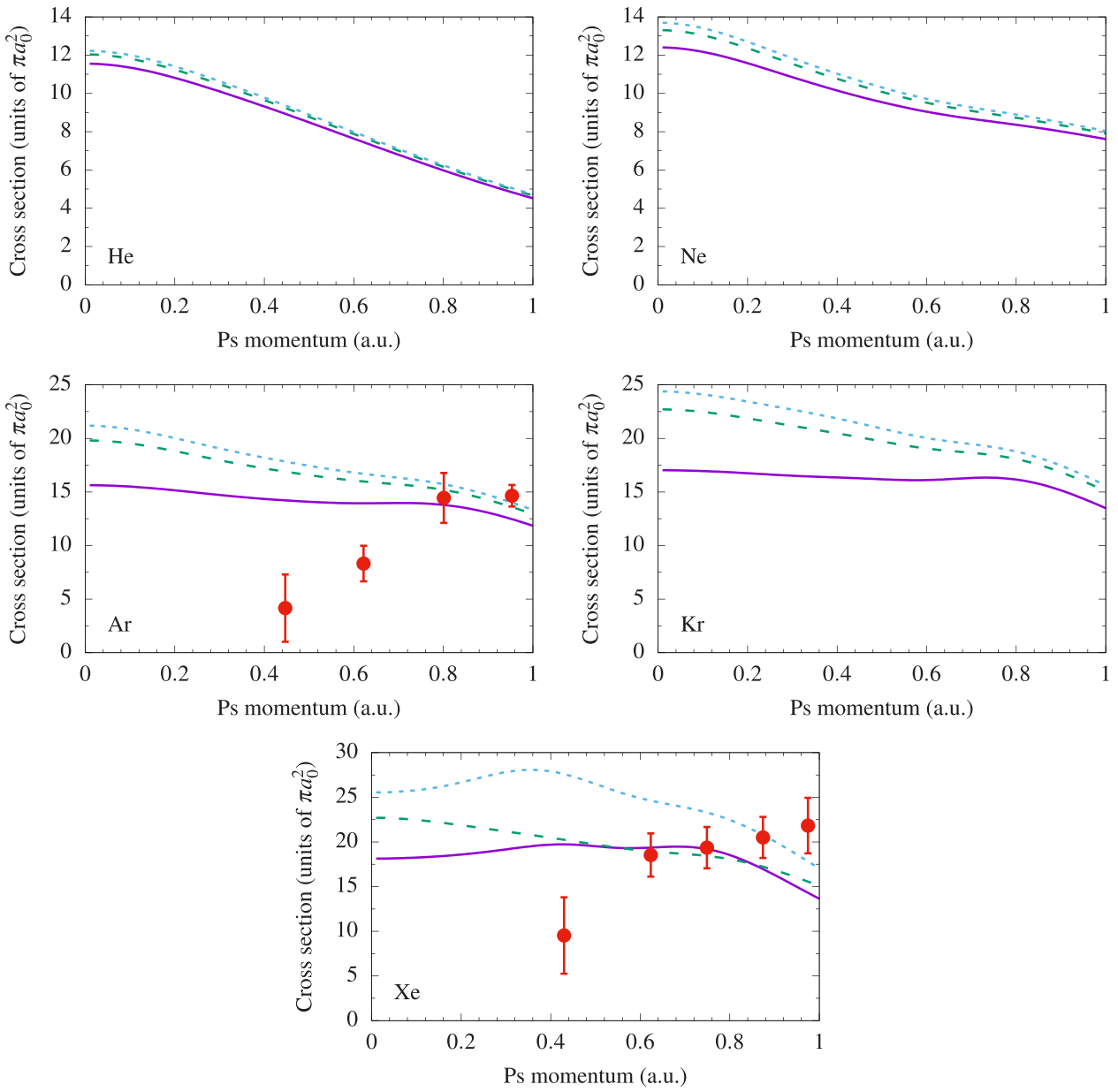

FIG. 9. Elastic scattering cross sections for Ps scattering on He, Ne, Ar, Kr, and Xe, with the electron and positron self-energy diagrams and screening diagrams being calculated at various energies E. Solid purple lines, $E = 0$; dashed green lines, $E = -0.25$ a.u.; dotted blue lines, $E = -0.375$ a.u. The red circles are the experimental measurements by Brawley *et al.* [28].

in the denominators of the corresponding diagrams should be negative, rather than zero. This is investigated in Sec. IV C.

(2) We may have overestimated the effect of short-range electron-positron correlations, i.e., the enhancement factors in Table I could be too large. This could be partly due to using enhancement factors calculated using Hartree-Fock states rather than Dyson states. However, using the Dyson enhancement factors instead would still give values of ${}^1Z_{\rm eff}$ significantly larger than experiment for Ar, Kr, and Xe. For example, for Xe, the enhancement factor that most significantly reduces in switching from Hartree-Fock to Dyson states is for an s-wave positron annihilating on the $5p$ orbital; its value changes from 9.26 to $\approx$6 [34]. Crudely scaling our current value of ${}^1Z_{\rm eff}(0)$ by a factor of $6/9.26 \approx 0.65$ gives ${}^1Z_{\rm eff}(0) \approx 0.61$, still 30% larger than the experimental value of 0.48 [74]. And if we were to correctly change the enhancement factors for each orbital and partial wave to their Dyson values separately, we would obtain a value even larger, as the enhancement factors for higher partial waves and/or core orbitals change less significantly.

(3) The enhancement factors that were used were calculated for zero energy of the positron. However, when the positron is "packaged" within Ps, the positron states in the expansion (18) of the Ps wave function cover a range of energies. It is possible that the contributions of higher-energy positron states should not be enhanced to the same degree as those of the lower-energy states. However, it is not clear why this effect would be more important for the heavier noble-gas atoms.

C. Dependence of results on energy used in energy denominators of diagrams

As we noted in Sec. II E, the self-energy of the electron or positron in the field of the atom and the screening corrections to the electron-positron Coulomb interaction within Ps, depend on the energy E, which appears in the energy denominators of the Goldstone diagrams. Up to this point, the self-energy and screening diagrams were calculated consistently using $E = 0$. We now briefly investigate how changing the value of E affects the scattering cross section and value of ${}^1Z_{\rm eff}(0)$ for each atom.

The true value of E in the energy denominators should be $E = K^2/4 - 1/4 - \Delta E$, where K is the Ps center-of-mass momentum, $-\frac{1}{4}$ a.u. is the internal energy of ground-state Ps, and ΔE estimates the typical excitation energy of the electron or positron within Ps. Thus, for low-energy collisions ($K \approx 0$), the electron and positron self-energy diagrams and the screening corrections should be calculated for a negative energy of -0.25 a.u., or lower. One can compute the mean value of ΔE for either the electron or positron in a particular Ps eigenstate in the cavity by

$$\langle \Delta E \rangle = \begin{cases} \sum_{\mu,\nu} |C_{\mu\nu}|^2 \varepsilon_\mu & \text{(electron)} \\ \sum_{\mu,\nu} |C_{\mu\nu}|^2 \varepsilon_\nu & \text{(positron)}, \end{cases} \tag{33}$$

where the $C_{\mu\nu}$ are the expansion coefficients in Eq. (18), and ε_μ (ε_ν) is the energy of electron (positron) state ψ_μ (ψ_ν). We calculated $\langle \Delta E \rangle$ for the electron and positron for the lowest-energy Ps eigenstates for He, Ar, and Xe (obtained with $E = 0$), and found values in the range 0.125–0.15 a.u. This value could be expected for ground-state Ps. Indeed, for a sufficiently large cavity, the Ps is quasifree, and the potential energy for the electron or positron is mostly due to the Coulomb interaction with the other particle. The expected values of the Ps kinetic energy T and potential energy V satisfy the virial theorem, $2\langle T \rangle = -\langle V \rangle$, so the total energy of the electron-positron pair is $\langle T \rangle + \langle V \rangle = \langle V \rangle/2$. This shows that for Ps with a small center-of-mass momentum $K \approx 0$, the expected value of the potential energy should be -0.5 a.u. (since the total Ps energy is just the internal energy, -0.25 a.u.). Assuming that the electron and positron have approximately the same mean excitation energy $\langle \Delta E \rangle$, we find $2\langle \Delta E \rangle - 0.5 \approx -0.25$, which gives $\langle \Delta E \rangle \approx 0.125$ a.u.

Taking into account the above considerations, we investigate the sensitivity of the scattering cross sections and ${}^1Z_{\rm eff}$ on the value of E, by calculating the self-energy and screening diagrams at $E = -0.25$ a.u. and $E = -0.375$ a.u., in addition to the value of $E = 0$ used previously.

Figure 9 shows the elastic cross sections for Ps scattering on He, Ne, Ar, Kr, and Xe for $E = 0$, -0.25, and -0.375 a.u. It is clear that for each atom, making the value of E more negative results in a larger cross section (although for Xe, in the momentum range $K \approx 0.6$–0.85 a.u., the $E = -0.25$ a.u. cross section is smaller than the $E = 0$ cross section, due to the delicate interplay of the S- and P-wave contributions). This occurs because making the energy denominators in the Goldstone diagrams more negative reduces their overall magnitude. This weakens the van der Waals-type attraction between Ps and the target atom, resulting in more negative phase shifts and a larger scattering length. The change in the cross section due to varying the value of E is more pronounced at low Ps momenta K and for heavier target atoms. For He, changing the value of E from 0 to -0.375 a.u. increases the cross section at $K = 0$ by only 6%, while the corresponding increase for Xe is 40%. This difference is due to characteristic atomic excitations energies [e.g., $\varepsilon_\mu - \varepsilon_n$ in Eq. (7)] being smaller in the heavier noble-gas atoms that have smaller ionization potentials, making the expressions for the diagrams more sensitive to the choice of E. Despite the visible change for all atoms, the basic shape of the cross section remains the same for all values of E, and agreement with the experimental data [28] is not improved.

TABLE IV. Values of ${}^1Z_{\rm eff}(0)$, calculated using many-body theory with vertex enhancement, using various energies E in the calculation of the self-energy and screening diagrams. Also shown are the experimental values. Our recommended values are shown in bold.

	E (a.u.)			
Atom	0	−0.25	−0.375	Expt. [35,74]
He	0.131	0.127	**0.124**	0.125
Ne	0.255	0.239	**0.231**	0.235
Ar	0.516	0.409	**0.375**	0.314
Kr	0.678	0.497	**0.446**	0.36
Xe	0.939	0.607	**0.530**	0.48

Table IV shows the vertex-enhanced values of ${}^1Z_{\rm eff}(0)$ for He, Ne, Ar, Kr, and Xe for $E = 0$, -0.25, and -0.375 a.u. As expected, making E more negative reduces the values of ${}^1Z_{\rm eff}(0)$, since it results in a more repulsive Ps-atom interaction. As with the cross sections, this effect is stronger in the heavier noble-gas atoms. The values of ${}^1Z_{\rm eff}(0)$ calculated for He and Ne with $E = -0.375$ a.u. are in near-perfect agreement with experiment [35]. For Ar, Kr, and Xe, the calculated values still overestimate the experimental data [35,74] by factors of 1.2, 1.2, and 1.1, respectively, but represent a very significant improvement on the values calculated with $E = 0$.

V. CONCLUSIONS

We have developed a many-body-theory approach to studying low-energy Ps interactions with noble-gas atoms. The entire Ps-atom system was enclosed in a hard-wall spherical cavity. The Dyson equation was solved separately for the electron and positron moving in the field of the target atom, and the resulting states were used to construct the two-particle Ps wave function. Construction of the Ps wave function in this manner ensured that distortion of both the target atom and the Ps were accurately accounted for. The two-particle Dyson equation was solved, and the energies and wave functions of the Ps eigenstates in the cavity were used to determine the scattering phase shifts (and hence the cross sections) and pickoff annihilation parameter ${}^1Z_{\rm eff}$.

Our calculations of the scattering cross section do not agree with the experimental data for Ar and Xe of Brawley *et al.* [28] that show a drop of the cross sections towards low Ps energies. In fact, we see that the general shape of each cross section is similar to that predicted by simpler calculations that mimicked

distortion of the target atom using a long-range model van der Waals potential [20]. The many-body-theory and van der Waals calculations generally come into good agreement for Ps momenta greater than 0.5 a.u. (At lower momenta, the van der Waals cross sections are quite sensitive to the choice of cutoff radius used in the model potential [20].) Agreement with measurements of the momentum-transfer cross sections (at thermal, room-temperature energies and other data below $\approx$2 eV) is also found to be mixed, and the measurements by different experimental groups are not always consistent. For the lightest target, He, our results are close to those of the coupled-state [30] and stochastic variational [31,32] calculations.

Calculations of $^1Z_{\rm eff}$ in the frozen-target approximation (performed by constructing the Ps wave function from Hartree-Fock electron and positron states in the field of the target atom) gave values an order of magnitude below the experimental value, due to the neglect of the target-atom distortion and short-range electron-positron correlations. Accounting for target-atom distortion by using the electron and positron Dyson states (i.e., including their self-energy) and the screening correction to their Coulomb interaction, and accounting for the short-range electron positron correlations by scaling the atomic-orbital—and positron-partial-wave–specific contributions to $^1Z_{\rm eff}$ by the annihilation vertex enhancement factors from Ref. [34], gives values of $^1Z_{\rm eff}$ in very close agreement with experiment for He and Ne, and within a factor of two for Ar, Kr, and Xe.

Finally, we investigated the effect of changing the energy E at which the electron and positron self-energy diagrams and screening corrections to the electron-positron Coulomb interaction were calculated. In addition to the data obtained for $E = 0$, the calculations were repeated for $E = -0.25$ and -0.375 a.u. Making E more negative results in a more repulsive Ps-atom interaction, and leads to somewhat larger scattering cross sections and smaller $^1Z_{\rm eff}$ values. Going from $E = 0$ to $E = -0.375$ a.u. increases the zero-energy cross section, from 6% for He to 40% for Xe. However, the basic shape of the cross sections is unchanged, and the discrepancy with the experimental data for Ar and Xe [28] persists. For the pickoff annihilation parameter $^1Z_{\rm eff}$, going from $E = 0$ to $E = -0.375$ a.u., leads to a decrease in $^1Z_{\rm eff}(0)$, from 5% for He to 45% for Xe. This brings the values of $^1Z_{\rm eff}$ for He and Ne into near-exact agreement with experiment [35] and within a factor of 1.2 of experiment [35,74] for Ar, Kr, and Xe. For He our result is within 4% of the stochastic variational calculation [32]. For Ne, Ar, Kr and Xe, our calculations of $^1Z_{\rm eff}$ are the only ones available that account for the Ps-atom dispersion forces and short-range electron-positron correlation effects, and thus serve as current benchmarks.

The work presented here represents a major step towards understanding low-energy Ps-atom interactions: virtual target-atom excitations have now been included in Ps scattering by many-electron atoms, and short-range electron-positron correlations have been accounted for in $^1Z_{\rm eff}$. However, there are many ways in which the calculations could be improved and extended. In the self-energy expansion for the electron-atom interaction, only diagrams up to second order in the electron-electron Coulomb interaction were included; similarly, only second-order diagrams were included in the screening correction to the electron-positron Coulomb interaction within Ps. Although technically cumbersome, it is possible to include higher-order corrections (e.g., dressing the single- and two-particle propagators with infinite ladder series of screened interactions as done in Ref. [76], and/or calculating the annihilation vertex corrections *ab initio*, accounting for the positron being "packaged" within Ps) and check whether these significantly affect the Ps-atom scattering cross section and pickoff annihilation rate. Also, the many-body theory used in the calculations is nonrelativistic: all of the Goldstone diagrams were calculated using single-particle Hartree-Fock electron and positron orbitals. Although we expect relativistic corrections to be small for the Ps-atom problem, in principle, Dirac-Fock orbitals could be used to account for these effects. Furthermore, we have only considered elastic scattering of Ps by noble-gas atoms. By investigating the nature of higher-energy states of Ps in the field of the target atom within the cavity, it may be possible to obtain information about inelastic-scattering processes, e.g., excitation and/or ionization of the Ps and/or target atom. Lastly, accounting for the relativistic spin-orbit interaction should enable calculations of the cross section of spin-orbit quenching, a spin-changing collision that transforms long-lived ortho-Ps (with mean lifetime 142 ns) into short-lived para-Ps (with mean lifetime 0.125 ns). Such collisions have a significant effect on the fraction of Ps atoms that survive to thermalization in gases of heavier atoms [74,77].

The persisting discord between calculated low-energy Ps-atom scattering cross sections and experimental data is a cause for concern. From the point of view of theory, observing a Ramsauer-Townsend minimum in the cross section, as predicted for Ar and Xe in Ref. [28], would require the overall Ps-atom interaction at low energy to be attractive (indicated by a positive S-wave phase shift and a negative scattering length), becoming repulsive at intermediate energies (indicated by the S-wave phase shift becoming negative). However, the level of agreement we obtained with experiment for $^1Z_{\rm eff}$ leads us to believe that our many-body-theory approach broadly captures the essential physics of the Ps-atom system correctly. We hope that ongoing theoretical and experimental investigations will resolve the discrepancies for the cross sections in the near future.

ACKNOWLEDGMENTS

This work has been supported by the Department for the Economy, Northern Ireland, UK (A.R.S.), the EPSRC UK, Grants No. EP/R006431/1 (A.R.S. and G.F.G.) and No. EP/N007948/1 (D.G.G.), and the European Research Council (ERC) StG 804383 (D.G.G.).

APPENDIX A: ANALYTICAL EXPRESSIONS FOR GOLDSTONE DIAGRAMS AND QUANTITIES DERIVED FROM Ps WAVE FUNCTION

In calculating the various diagrams in $\langle\varepsilon'|\Sigma_E|\varepsilon\rangle$ and $\langle\varepsilon'|\delta V_E|\varepsilon\rangle$, integration over the angular variables is performed analytically [78]. The Coulomb matrix element $\pm\langle\nu'\mu'|V|\mu\nu\rangle$ for two particles coupled to an angular momentum J [see

Eq. (8)] is given by

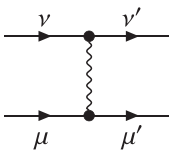

$$= \pm\langle\nu'\mu'|V^{(J)}|\mu\nu\rangle = \pm\sum_{l=0}^{\infty}(-1)^{J+l}\begin{Bmatrix} J & l_{\mu'} & l_{\nu'} \\ l & l_\nu & l_\mu \end{Bmatrix}\langle\nu'\mu'\|V_l\|\mu\nu\rangle, \tag{A1}$$

where we choose the positive (negative) sign for a repulsive (attractive) Coulomb interaction, the quantity in braces is a $6j$ symbol, the sum over l is actually finite (with the allowed values determined by the selection rules of the $6j$ symbol),

$$\langle\nu'\mu'\|V_l\|\mu\nu\rangle = \sqrt{[l_{\nu'}][l_{\mu'}][l_\mu][l_\nu]}\begin{pmatrix} l_{\nu'} & l & l_\nu \\ 0 & 0 & 0 \end{pmatrix}\begin{pmatrix} l_{\mu'} & l & l_\mu \\ 0 & 0 & 0 \end{pmatrix}\int_0^{R_c}\int_0^{R_c} P_{\varepsilon_{\nu'}l_{\nu'}}(r')P_{\varepsilon_{\mu'}l_{\mu'}}(r)\frac{r_<^l}{r_>^{l+1}}P_{\varepsilon_\mu l_\mu}(r)P_{\varepsilon_\nu l_\nu}(r')drdr', \tag{A2}$$

is the reduced Coulomb matrix element, $[l] \equiv 2l+1$, $r_< = \min(r, r')$, $r_> = \max(r, r')$, and the quantities in parentheses are $3j$ symbols.

We now give expressions for the various Goldstone diagrams. Note that sums over magnetic quantum numbers and spins have already been carried out, so that sums over intermediate states only pertain to the radial and orbital quantum numbers, e.g., $\sum_\mu \equiv \sum_{\varepsilon_\mu, l_\mu}$. For convenience, we define the following quantities which occur regularly:

$$\langle\nu'\mu'\|V^{(l)}\|\mu\nu\rangle = \sum_{l'=0}^{\infty}(-1)^{l+l'}\begin{Bmatrix} l & l_{\mu'} & l_{\nu'} \\ l' & l_\nu & l_\mu \end{Bmatrix}\langle\nu'\mu'\|V_{l'}\|\mu\nu\rangle, \tag{A3}$$

$$\langle\nu'\mu'\|\widetilde{V}^{(l)}\|\mu\nu\rangle = \sum_{l'=0}^{\infty}(-1)^{l+l'}\begin{Bmatrix} l & l_{\mu'} & l_\nu \\ l' & l_{\nu'} & l_\mu \end{Bmatrix}\langle\nu'\mu'\|V_{l'}\|\mu\nu\rangle, \tag{A4}$$

$$\langle\nu'\mu'\|\Gamma_E^{(l)}\|\mu\nu\rangle = -\langle\nu'\mu'\|V^{(l)}\|\mu\nu\rangle - \sum_{\mu'',\nu''}\frac{\langle\nu'\mu'\|V^{(l)}\|\mu''\nu''\rangle\langle\nu''\mu''\|\Gamma_E^{(l)}\|\mu\nu\rangle}{E - \varepsilon_{\mu''} - \varepsilon_{\nu''} + i\delta}. \tag{A5}$$

Note the different positions of l_ν and $l_{\nu'}$ in the $6j$ symbols in Eqs. (A3) and (A4). Equation (A5) is a linear matrix equation that can be solved to find the reduced ladder matrix elements $\langle\nu'\mu'\|\Gamma_E^{(l)}\|\mu\nu\rangle$. The expressions for the self-energy and screening diagrams are as follows:

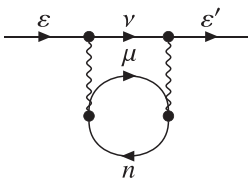

$$= \sum_{\substack{\mu,\nu>F \\ n\leqslant F}}\sum_l \frac{2}{[l][l_\varepsilon]}\frac{\langle\varepsilon' n\|V_l\|\mu\nu\rangle\langle\nu\mu\|V_l\|n\varepsilon\rangle}{E + \varepsilon_n - \varepsilon_\mu - \varepsilon_\nu + i\delta}, \tag{A6}$$

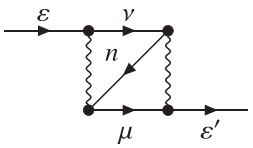

$$= -\sum_{\substack{\mu,\nu>F \\ n\leqslant F}}\sum_l \frac{1}{[l_\varepsilon]}\frac{\langle n\varepsilon'\|\widetilde{V}^{(l)}\|\mu\nu\rangle\langle\nu\mu\|V_l\|n\varepsilon\rangle}{E + \varepsilon_n - \varepsilon_\mu - \varepsilon_\nu + i\delta}, \tag{A7}$$

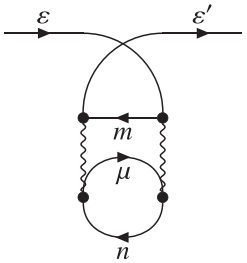

$$= -\sum_{\substack{\mu>F \\ m,n\leqslant F}}\sum_l \frac{2}{[l][l_\varepsilon]}\frac{\langle\varepsilon'\mu\|V_l\|nm\rangle\langle mn\|V_l\|\mu\varepsilon\rangle}{-E + \varepsilon_m + \varepsilon_n - \varepsilon_\mu + i\delta}, \tag{A8}$$

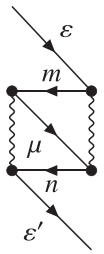

$$= \sum_{\substack{\mu>F \\ m,n\leqslant F}} \sum_{l} \frac{1}{[l_\varepsilon]} \frac{\langle \mu\varepsilon' \| \widetilde{V}^{(l)} \| nm \rangle \langle mn \| V_l \| \mu\varepsilon \rangle}{-E + \varepsilon_m + \varepsilon_n - \varepsilon_\mu + i\delta}, \tag{A9}$$

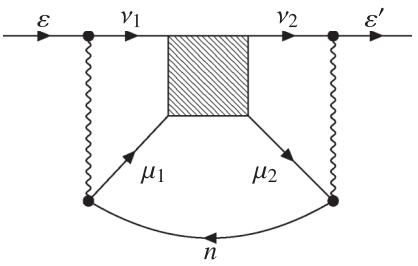

$$= \sum_{\substack{\mu_1,\mu_2>F \\ n\leqslant F}} \sum_{\nu_1,\nu_2} \sum_{l} \frac{2[l]}{[l_\varepsilon]} \frac{\langle \varepsilon' n \| V^{(l)} \| \mu_2\nu_2 \rangle \langle \nu_2\mu_2 \| \Gamma^{(l)}_{E+\varepsilon_n} \| \mu_1\nu_1 \rangle \langle \nu_1\mu_1 \| V^{(l)} \| n\varepsilon \rangle}{(E + \varepsilon_n - \varepsilon_{\mu_1} - \varepsilon_{\nu_1})(E + \varepsilon_n - \varepsilon_{\mu_2} - \varepsilon_{\nu_2})}, \tag{A10}$$

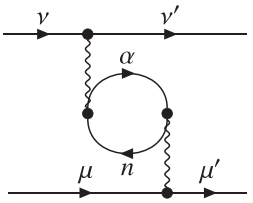

$$= -\sum_{\substack{\alpha>F \\ n\leqslant F}} \sum_{l} \frac{1}{[l]} \frac{\langle n\mu' \| V_l \| \mu\alpha \rangle \langle \alpha\nu' \| V_l \| \nu n \rangle}{E + \varepsilon_n - \varepsilon_\alpha + i\delta}, \tag{A11}$$

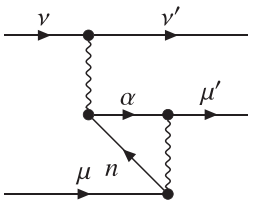

$$= \sum_{\substack{\alpha>F \\ n\leqslant F}} \sum_{l} \frac{\langle \mu' n \| \widetilde{V}^{(l)} \| \mu\alpha \rangle \langle \alpha\nu' \| V_l \| \nu n \rangle}{E + \varepsilon_n - \varepsilon_\alpha + i\delta}, \tag{A12}$$

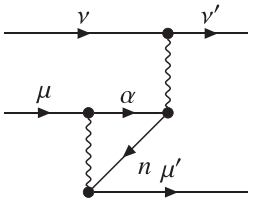

$$= \sum_{\substack{\alpha>F \\ n\leqslant F}} \sum_{l} \frac{\langle \mu'\alpha \| \widetilde{V}^{(l)} \| \mu n \rangle \langle n\nu' \| V_l \| \nu\alpha \rangle}{E + \varepsilon_n - \varepsilon_\alpha + i\delta}, \tag{A13}$$

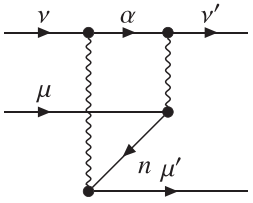

$$= -\sum_{n\leqslant F} \sum_{\alpha} \sum_{l,l',l''} (-1)^{l_\alpha + l_n} [l] \begin{Bmatrix} l_{\mu'} & l & l_\mu \\ l' & l_\alpha & l'' \end{Bmatrix} \begin{Bmatrix} l_{\nu'} & l & l_\nu \\ l'' & l_n & l' \end{Bmatrix} \frac{\langle \nu' n \| V_{l'} \| \mu\alpha \rangle \langle \alpha\mu' \| V_{l''} \| n\nu \rangle}{E + \varepsilon_n - \varepsilon_\alpha + i\delta}. \tag{A14}$$

The two-particle Ps wave function (18) is written explicitly in terms of the single-particle electron and positron basis states as

$$\Psi_{J^\Pi}(\mathbf{r}_e, \mathbf{r}_p) = \frac{1}{r_e r_p} \sum_{\substack{\varepsilon_\mu, l_\mu \\ \varepsilon_\nu, l_\nu}} C^{(J^\Pi)}_{\varepsilon_\mu l_\mu \varepsilon_\nu l_\nu} \mathcal{P}_{\varepsilon_\mu l_\mu}(r_e) \mathcal{P}_{\varepsilon_\nu l_\nu}(r_p) \sum_{m_\mu, m_\nu} C^{JM}_{l_\mu m_\mu l_\nu m_\nu} Y_{l_\mu m_\mu}(\hat{\mathbf{r}}_e) Y_{l_\nu m_\nu}(\hat{\mathbf{r}}_p), \tag{A15}$$

where $C^{(J^\Pi)}_{\varepsilon_\mu l_\mu \varepsilon_\nu l_\nu}$ is an expansion coefficient and $C^{JM}_{l_\mu m_\mu l_\nu m_\nu}$ is a Clebsch-Gordan coefficient.[5] Besides the selection rules due to the Clebsch-Gordan coefficient, the summation is restricted by parity, $(-1)^{l_\mu + l_\nu} = \Pi$, where $\Pi = 1$ (-1) for the even (odd) states.

[5]Comparing Eq. (A15) with Eq. (18), $C_{\mu\nu} \equiv C^{(J^\Pi)}_{\varepsilon_\mu l_\mu \varepsilon_\nu l_\nu} C^{JM}_{l_\mu m_\mu l_\nu m_\nu}$.

TABLE V. Parameters for the effective-range fits (B2), (B3), and (B4) for the S-, P-, and D-wave phase shifts δ_L.

		Atom				
L	Parameter	He	Ne	Ar	Kr	Xe
0	α_0	−0.588	−0.568	−0.506	−0.485	−0.470
	α_1	0.312	0.323	0.772	0.921	1.22
1	α_0	−1.90	−2.31	−2.16	−2.35	−2.38
	α_1	3.41	2.86	0.439	0.167	−0.607
	α_2	2.92	0.138	0.940	1.04	1.61
2	α_0	1.01	1.18	3.46	5.15	9.65
	α_1	−1.73	−2.25	−5.78	−8.52	−15.5
	α_2	22.4	8.19	11.7	14.4	29.8

We now consider the calculation of ${}^1Z_{\rm eff}$. The density of the atomic electrons is

$$\rho(\mathbf{r}) = \sum_{n\leqslant F} |\psi_n(\mathbf{r})|^2 = 2\sum_{\varepsilon_n,l_n} \frac{[l_n]}{4\pi}\frac{\mathcal{P}_{\varepsilon_n l_n}(r)^2}{r^2}, \tag{A16}$$

where the factor of two accounts for summation over the spins. Assuming that the electron and positron in Ps are coupled to an angular momentum of $J=0$, substituting Eq. (A16) into Eq. (22), and carrying out the angular integrals analytically, we obtain

$${}^1Z_{\rm eff} = \sum_{\varepsilon_n,l_n}\frac{[l_n]}{8\pi}\sum_{\varepsilon_\mu,\varepsilon_\nu,\varepsilon_{\nu'},l}\gamma_{nl}C^{(0^+)}_{\varepsilon_\mu l\varepsilon_\nu l}C^{(0^+)}_{\varepsilon_\mu l\varepsilon_{\nu'} l}\int_0^{R_c}\mathcal{P}_{\varepsilon_n l_n}(r)^2\mathcal{P}_{\varepsilon_\nu l}(r)\mathcal{P}_{\varepsilon_{\nu'} l}(r)\frac{dr}{r^2}. \tag{A17}$$

The method of calculating the Ps center-of-mass density $\rho_{\rm cm}(\mathbf{r})$, Eq. (29), depends on whether $\mathbf{r}=\mathbf{0}$ or $\mathbf{r}\neq\mathbf{0}$. For $\mathbf{r}=\mathbf{0}$, the δ function can be expanded as

$$\delta\left(\frac{\mathbf{r}_e+\mathbf{r}_p}{2}-\mathbf{0}\right) = 8\frac{\delta(r_e-r_p)}{r_e^2}\sum_{l=0}^{\infty}(-1)^l\sum_{m=-l}^{l}Y^*_{lm}(\hat{\mathbf{r}}_e)Y_{lm}(\hat{\mathbf{r}}_p), \tag{A18}$$

giving

$$\rho_{\rm cm}(\mathbf{0}) = \sum_{\substack{\varepsilon_\mu,l_\mu\\ \varepsilon_\nu,l_\nu}}\sum_{\substack{\varepsilon_{\mu'},l_{\mu'}\\ \varepsilon_{\nu'},l_{\nu'}}} C^{(J^\Pi)}_{\varepsilon_\mu l_\mu\varepsilon_\nu l_\nu}C^{(J^\Pi)}_{\varepsilon_{\mu'} l_{\mu'}\varepsilon_{\nu'} l_{\nu'}}\sum_l(-1)^J\begin{Bmatrix} J & l_{\mu'} & l_{\nu'}\\ l & l_\nu & l_\mu\end{Bmatrix}\frac{2[l]}{\pi}\sqrt{[l_{\nu'}][l_{\mu'}][l_\mu][l_\nu]}\begin{pmatrix} l_{\nu'} & l & l_\nu\\ 0 & 0 & 0\end{pmatrix}\begin{pmatrix} l_{\mu'} & l & l_\mu\\ 0 & 0 & 0\end{pmatrix}$$
$$\times\int_0^{R_c}\mathcal{P}_{\varepsilon_{\nu'} l_{\nu'}}(r)\mathcal{P}_{\varepsilon_{\mu'} l_{\mu'}}(r)\mathcal{P}_{\varepsilon_\mu l_\mu}(r)\mathcal{P}_{\varepsilon_\nu l_\nu}(r)\frac{dr}{r^2}. \tag{A19}$$

For $\mathbf{r}\neq\mathbf{0}$, the δ function expands as

$$\delta\left(\frac{\mathbf{r}_e+\mathbf{r}_p}{2}-\mathbf{r}\right) = \frac{\delta(|\mathbf{r}_e+\mathbf{r}_p)|/2-r)}{r^2}\sum_{l=0}^{\infty}\frac{[l]}{4\pi}P_l(\cos\omega), \tag{A20}$$

where P_l is the Legendre polynomial and ω is the angle between $\mathbf{r}_e+\mathbf{r}_p$ and $\mathbf{r}$. A difficulty arises in that the δ function on the RHS of Eq. (A20) also needs to be expanded. For simplicity, we only consider the case where $J=0$. Then only the $l=0$ term on the RHS of Eq. (A20) is nonzero:

$$\delta\left(\frac{\mathbf{r}_e+\mathbf{r}_p}{2}-\mathbf{r}\right) = \frac{\delta(|\mathbf{r}_e+\mathbf{r}_p|/2-r)}{r^2}\frac{1}{4\pi}$$
$$= \frac{1}{2\pi r^2}\delta(|\mathbf{r}_e+\mathbf{r}_p|-2r). \tag{A21}$$

We now expand $\delta(|\mathbf{r}_e+\mathbf{r}_p|-2r)$ as

$$\delta(|\mathbf{r}_e+\mathbf{r}_p|-2r) = \sum_{l=0}^{\infty}\frac{[l]}{4\pi}g_l(r_e,r_p)P_l(\cos\omega), \tag{A22}$$

where the expansion coefficients g_l are to be determined. Multiplying both sides of Eq. (A22) by $P_{l'}(\cos\omega)\sin\omega$, integrating over ω from 0 to π, changing variables to $x\equiv\cos\omega$, and relabelling l' as l, we obtain

$$g_l(r_e,r_p) = 2\pi\int_{-1}^{1}\delta\left(\sqrt{r_e^2+r_p^2+2r_e r_p x}-2r\right)P_l(x)dx. \tag{A23}$$

We recall that a general property of the δ function is

$$\delta[f(x)] = \sum_i\frac{\delta(x-x_i)}{|f'(x_i)|}, \tag{A24}$$

where the x_i are the roots of $f(x)$. In this case we obtain

$$g_l(r_e, r_p) = \frac{4\pi r}{r_e r_p} \int_{-1}^{1} \delta\left(x - \frac{4r^2 - r_e^2 - r_p^2}{2r_e r_p}\right) P_l(x) dx, \tag{A25}$$

which gives

$$g_l(r_e, r_p) = \frac{4\pi r}{r_e r_p} P_l\left(\frac{4r^2 - r_e^2 - r_p^2}{2r_e r_p}\right) \tag{A26}$$

if $|r_e - r_p| < 2r < r_e + r_p$, and $g_l(r_e, r_p) = 0$ otherwise. Combining Eqs. (29), (A21), (A22), and (A26), and noting that for $J = 0$ we require $l_\mu = l_\nu$ and $l_{\mu'} = l_{\nu'}$, we obtain

$$\begin{aligned}\rho_{\rm cm}(\mathbf{r}) = &\sum_{\substack{\varepsilon_\mu, \varepsilon_\nu \\ \varepsilon_{\mu'}, \varepsilon_{\nu'}}} \sum_{l_\mu, l_{\mu'}} C^{(0^+)}_{\varepsilon_\mu l_\mu \varepsilon_\nu l_\mu} C^{(0^+)}_{\varepsilon_{\mu'} l_{\mu'} \varepsilon_{\nu'} l_{\mu'}} (-1)^{l_\mu + l_{\mu'}} \sqrt{[l_\mu][l_{\mu'}]} \\ &\times \sum_l [l] \begin{pmatrix} l_{\mu'} & l & l_\mu \\ 0 & 0 & 0 \end{pmatrix}^2 \frac{1}{2\pi r} \\ &\times \int_0^{R_c} \int_{|2r - r_p|}^{\min(2r + r_p, R_c)} \mathcal{P}_{\varepsilon_{\nu'} l_{\mu'}}(r_p) \mathcal{P}_{\varepsilon_{\mu'} l_{\mu'}}(r_e) \\ &\times P_l\left(\frac{4r^2 - r_e^2 - r_p^2}{2r_e r_p}\right) \mathcal{P}_{\varepsilon_\mu l_\mu}(r_e) \mathcal{P}_{\varepsilon_\nu l_\mu}(r_p) \frac{dr_e}{r_e} \frac{dr_p}{r_p}.\end{aligned} \tag{A27}$$

APPENDIX B: EFFECTIVE-RANGE THEORY FITS FOR SCATTERING PHASE SHIFTS

The Ps scattering phase shifts are determined from the Ps energy eigenvalues using the boundary condition on the Ps center-of-mass motion at the cavity wall, as described in Ref. [20]. Calculations were performed using cavity radii of 10, 12, 14, and 16 a.u. Effective-range-type fits were used to interpolate the S, P, and D phase shifts calculated at the discrete values of the Ps center-of-mass momentum K. These fits were used to determine the scattering length and the partial contributions to the elastic and momentum-transfer cross sections. Here we detail the fits for the phase shifts.

At low momenta K, the S-wave phase shift δ_0 behaves according to

$$K \cot \delta_0 \simeq -\frac{1}{A} + \frac{1}{2} r_0 K^2, \tag{B1}$$

where A is the scattering length and r_0 is the effective range [79]. This can be rearranged to give

$$\delta_0(K) = \tan^{-1} \frac{K}{\alpha_0 + \alpha_1 K^2} \quad (\mathrm{mod}\, \pi), \tag{B2}$$

where $\alpha_0 = -1/A$ and $\alpha_1 = r_0/2$. The P- and D-wave phase shifts behave according to

$$\begin{aligned}\delta_1 &= \alpha K^3 + \beta K^4 + \gamma K^5 + \varepsilon K^7 \ln K + O\big(K^7\big), \\ \delta_2 &= \zeta K^4 + \eta K^5 + \lambda K^7 + \mu K^9 \ln K + O(K^9),\end{aligned}$$

respectively, where α, β, γ, ε, ζ, η, λ, and μ are constants [79]. We found that simple polynomial fits obtained by truncating these expansions tend to grow too large as $K \to 1$ a.u., so we used the following Padé-type fits instead:

$$\delta_1(K) = \frac{\alpha_0 K^3}{1 + \alpha_1 K^2 + \alpha_2 K^4}, \tag{B3}$$

$$\delta_2(K) = \frac{\alpha_0 K^4 + \alpha_1 K^5}{1 + \alpha_2 K^6}. \tag{B4}$$

These fits have the correct leading-order behavior as $K \to 0$ and vary relatively slowly at large K, as observed in the calculated phase shifts. Table V shows the values of the parameters of the fits for δ_L ($L = 0$, 1, 2) for He, Ne, Ar, Kr, and Xe.

[1] G. Laricchia and H. R. J. Walters, Positronium collision physics, Riv. Nuovo. Cimento **35**, 305 (2012).

[2] A. Kellerbauer, M. Amoretti, A. Belov, G. Bonomi, I. Boscolo, R. Brusa, M. Büchner, V. Byakov, L. Cabaret, C. Canali, C. Carraro, F. Castelli, S. Cialdi, M. de Combarieu, D. Comparat, G. Consolati, N. Djourelov, M. Doser, G. Drobychev, A. Dupasquier *et al.*, Proposed antimatter gravity measurement with an antihydrogen beam, Nucl. Instrum. Methods Phys. Res., Sect. B **266**, 351 (2008).

[3] P. Debu (GBAR collaboration), Gravitational behavior of antihydrogen at rest, Hyperfine Interact. **212**, 51 (2012).

[4] P. Pérez, D. Banerjee, F. Biraben, D. Brook-Roberge, M. Charlton, P. Cladé, P. Comini, P. Crivelli, O. Dalkarov, P. Debu, A. Douillet, G. Dufour, P. Dupré, S. Eriksson, P. Froelich, P. Grandemange, S. Guellati, R. Guérout *et al.*, The GBAR antimatter gravity experiment, Hyperfine Interact. **233**, 21 (2015).

[5] C. Amsler, M. Antonello, A. Belov, G. Bonomi, R. S. Brusa, M. Caccia, A. Camper, R. Caravita, F. Castelli, P. Cheinet, D. Comparat, G. Consolati, A. Demetrio, L. D. Noto, M. Doser, M. Fanì, R. Ferragut, J. Fesel, S. Gerber *et al.*, Pulsed production of antihydrogen, Commun. Phys. **4**, 19 (2021).

[6] G. Consolati, R. Ferragut, A. Galarneau, F. Di Renzo, and F. Quasso, Mesoporous materials for antihydrogen production, Chem. Soc. Rev. **42**, 3821 (2013).

[7] D. W. Gidley, H. Peng, and R. S. Vallery, Positron annihilation as a method to characterize porous materials, Riv. Nuovo. Cimento **36**, 49 (2006).

[8] K. Shibuya, T. Nakayama, H. Saito, and T. Hyodo, Spin conversion and pick-off annihilation of ortho-positronium in gaseous xenon at elevated temperatures, Phys. Rev. A **88**, 012511 (2013).

[9] K. Shibuya, Y. Kawamura, and H. Saito, Time-resolved determination of ortho-positronium kinetic energy utilizing p-wave scattering during positronium-xenon collisions, Phys. Rev. A **88**, 042517 (2013).

[10] K. Shibuya and H. Saito, Partial-wave analysis for positronium-xenon collisions in the ultralow-energy region, Phys. Rev. A **97**, 052702 (2018).

[11] D. B. Cassidy and A. P. Mills, Jr., The production of molecular positronium, Nature (London) **449**, 195 (2007).

[12] D. B. Cassidy and A. P. Mills, Jr., Interactions Between Positronium Atoms in Porous Silica, Phys. Rev. Lett. **100**, 013401 (2008).

[13] D. B. Cassidy and A. P. Mills, Jr., Enhanced Ps-Ps Interactions due to Quantum Confinement, Phys. Rev. Lett. **107**, 213401 (2011).

[14] D. B. Cassidy, T. H. Hisakado, H. W. K. Tom, and A. P. Mills, Jr., Optical Spectroscopy of Molecular Positronium, Phys. Rev. Lett. **108**, 133402 (2012).

[15] P. M. Platzman and A. P. Mills, Possibilities for Bose condensation of positronium, Phys. Rev. B **49**, 454 (1994).

[16] A. P. Mills, Jr., Chemistry and physics with many positrons, Radiat. Phys. Chem. **76**, 76 (2007).

[17] D. B. Cassidy and A. P. Mills, Jr., Physics with dense positronium, Phys. Status Solidi C **4**, 3419 (2007).

[18] D. B. Cassidy and S. D. Hogan, Atom control and gravity measurements using Rydberg positronium, Int. J. Mod. Phys.: Conf. Ser. **30**, 1460259 (2014).

[19] A. R. Swann, D. B. Cassidy, A. Deller, and G. F. Gribakin, Formation of positron-atom bound states in collisions between Rydberg Ps and neutral atoms, Phys. Rev. A **93**, 052712 (2016).

[20] A. R. Swann and G. F. Gribakin, Calculations of positronium-atom scattering using a spherical cavity, Phys. Rev. A **97**, 012706 (2018).

[21] J. E. Blackwood, C. P. Campbell, M. T. McAlinden, and H. R. J. Walters, Positronium scattering by helium, Phys. Rev. A **60**, 4454 (1999).

[22] J. E. Blackwood, M. T. McAlinden, and H. R. J. Walters, Positronium scattering by Ne, Ar, Kr and Xe in the frozen target approximation, J. Phys. B: At., Mol. Opt. Phys. **35**, 2661 (2002).

[23] J. E. Blackwood, M. T. McAlinden, and H. R. J. Walters, Reply to comment on "Positronium scattering by Ne, Ar, Kr and Xe in the frozen target approximation," J. Phys. B: At., Mol. Opt. Phys. **36**, 797 (2003).

[24] J. Mitroy and I. A. Ivanov, Positronium scattering from closed-shell atoms and ions, Phys. Rev. A **65**, 012509 (2001).

[25] J. Mitroy and M. W. J. Bromley, Positronium scattering from Kr and Xe and low energies, Phys. Rev. A **67**, 034502 (2003).

[26] I. I. Fabrikant and G. F. Gribakin, Positronium-atom scattering at low energies, Phys. Rev. A **90**, 052717 (2014).

[27] G. F. Gribakin, A. R. Swann, R. S. Wilde, and I. I. Fabrikant, Positronium collisions with rare-gas atoms, J. Phys. B: At., Mol. Opt. Phys. **49**, 064004 (2016).

[28] S. J. Brawley, S. E. Fayer, M. Shipman, and G. Laricchia, Positronium Production and Scattering below Its Breakup Threshold, Phys. Rev. Lett. **115**, 223201 (2015).

[29] D. G. Green, A. R. Swann, and G. F. Gribakin, Many-Body Theory for Positronium-Atom Interactions, Phys. Rev. Lett. **120**, 183402 (2018).

[30] H. R. J. Walters, A. C. H. Yu, S. Sahoo, and S. Gilmore, Positronium-atom collisions, Nucl. Instrum. Meth. Phys. Res., Sect. B **221**, 149 (2004).

[31] J. Y. Zhang and J. Mitroy, Stochastic variational method for elastic scattering, Phys. Rev. A **78**, 012703 (2008).

[32] M.-S. Wu, J.-Y. Zhang, X. Gao, Y. Qian, H.-H. Xie, K. Varga, Z.-C. Yan, and U. Schwingenschlögl, Confined variational calculation of *o*-Ps–He scattering properties, Phys. Rev. A **101**, 042705 (2020).

[33] D. G. Green and G. F. Gribakin, γ Spectra and Enhancement Factors for Positron Annihilation with Core Electrons, Phys. Rev. Lett. **114**, 093201 (2015).

[34] D. G. Green and G. F. Gribakin, Enhancement factors for positron annihilation on valence and core orbitals of noble-gas atoms, in *Concepts, Methods and Applications of Quantum Systems in Chemistry and Physics,* edited by Y. Wang, M. Thachuk, R. Krems, and J. Maruani, Progress in Theoretical Chemistry and Physics (Springer, Cham, 2018), Vol. 31, p. 243.

[35] M. Charlton, Experimental studies of positrons scattering in gases, Rep. Prog. Phys. **48**, 737 (1985).

[36] R. Brown, Q. Prigent, A. R. Swann, and G. F. Gribakin, Effective radius of ground- and excited-state positronium in collisions with hard walls, Phys. Rev. A **95**, 032705 (2017).

[37] A. L. Fetter and J. D. Walecka, *Quantum Theory of Many-Particle Systems* (McGraw-Hill, New York, 1971).

[38] J. Boyle and M. Pindzola, *Many-Body Atomic Physics* (Cambridge University Press, Cambridge, 1998).

[39] J. S. Bell and E. J. Squires, A Formal Optical Model, Phys. Rev. Lett. **3**, 96 (1959).

[40] G. F. Gribakin and J. A. Ludlow, Many-body theory of positron-atom interactions, Phys. Rev. A **70**, 032720 (2004).

[41] M. Amusia, N. Cherepkov, L. Chernysheva, and S. Shapiro, Elastic scattering of slow electrons and level shifts in Ar, Phys. Lett. A **46**, 387 (1974).

[42] M. Ya. Amus'ya, N. A. Cherepkov, L. V. Chernysheva, S. G. Shapiro, A. Tanchich, Elastic scattering of slow electrons by atoms, Zh. Eksp. Teor. Phys. **68**, 2023 (1975) [Sov. Phys. JETP **41**, 1012 (1975)].

[43] M. Y. Amusia, N. A. Cherepkov, L. V. Chernysheva, D. M. Davidović, and V. Radojević, Slow-electron elastic scattering on argon, Phys. Rev. A **25**, 219 (1982).

[44] W. R. Johnson and C. Guet, Elastic scattering of electrons from Xe, Cs^+, and Ba^{2+}, Phys. Rev. A **49**, 1041 (1994).

[45] W. R. Johnson and C. Guet, Erratum: Elastic scattering of electrons from Xe, Cs^+, and Ba^{2+} [Phys. Rev. A **49**, 1041 (1994)], Phys. Rev. A **64**, 019901(E) (2001).

[46] V. A. Dzuba, V. V. Flambaum, W. A. King, B. N. Miller, and O. P. Sushkov, Interaction between slow positrons and atoms, Phys. Scr. **T46**, 248 (1993).

[47] D. G. Green, J. A. Ludlow, and G. F. Gribakin, Positron scattering and annihilation on noble-gas atoms, Phys. Rev. A **90**, 032712 (2014).

[48] V. A. Dzuba, V. V. Flambaum, and M. G. Kozlov, Combination of the many-body perturbation theory with the configuration-interaction method, Phys. Rev. A **54**, 3948 (1996).

[49] P. A. Fraser and M. Kraidy, The pick-off quenching of orthopositronium in helium, Proc. Phys. Soc., London **89**, 533 (1966).

[50] E. Bonderup, J. U. Andersen, and D. N. Lowy, Enhancement of positron annihilation with core electrons, Phys. Rev. B **20**, 883 (1979).

[51] M. Ya. Amusia and L. V. Chernysheva, *Computation of Atomic Processes: A Handbook for the ATOM Programs* (IOP Publishing, Bristol, 1997).

[52] C. Schwartz, Importance of angular correlations between atomic electrons, Phys. Rev. **126**, 1015 (1962).

[53] C. Schwartz, in Methods in Computational Physics (Academic Press, New York, 1963), Vol. 2, pp. 241–266.

[54] W. Kutzelnigg and J. D. Morgan, Rates of convergence of the partial-wave expansions of atomic correlation energies, J. Chem. Phys. **96**, 4484 (1992).

[55] G. F. Gribakin and J. Ludlow, Convergence of partial-wave expansions for energies, scattering amplitudes and positron annihilation rates, J. Phys. B: At., Mol. Opt. Phys. **35**, 339 (2002).
[56] J. Mitroy, Effective range description of annihilating collisions, Phys. Rev. A **66**, 022716 (2002).
[57] S. Chiesa, M. Mella, and G. Morosi, Orthopositronium scattering off H and He, Phys. Rev. A **66**, 042502 (2002).
[58] K. F. Canter, J. D. McNutt, and L. O. Roellig, Positron annihilation in low-temperature rare gases. I. Helium, Phys. Rev. A **12**, 375 (1975).
[59] J. P. Hernandez, Self-trapping of ortho-positronium in dense fluid helium, Phys. Rev. A **14**, 1579 (1976).
[60] R. M. Nieminen, I. Välimaa, M. Manninen, and P. Hautojärvi, Density-functional theory of positronium and electron bubbles in helium fluids, Phys. Rev. A **21**, 1677 (1980).
[61] K. Rytsola, J. Vettenranta, and P. Hautojarvi, An experimental study of positronium bubbles in helium fluids, J. Phys. B: At. Mol. Phys. **17**, 3359 (1984).
[62] P. G. Coleman, S. Rayner, F. M. Jacobsen, M. Charlton, and R. N. West, Angular correlation studies of positron annihilation in the noble gases, J. Phys. B: At., Mol. Opt. Phys. **27**, 981 (1994).
[63] Y. Nagashima, T. Hyodo, K. Fujiwara, and A. Ichimura, Momentum-transfer cross section for slow positronium-He scattering, J. Phys. B: At., Mol. Opt. Phys. **31**, 329 (1998).
[64] J. J. Engbrecht, M. J. Erickson, C. P. Johnson, A. J. Kolan, A. E. Legard, S. P. Lund, M. J. Nyflot, and J. D. Paulsen, Energy-dependent Ps-He momentum-transfer cross section at low energies, Phys. Rev. A **77**, 012711 (2008).
[65] M. Skalsey, J. J. Engbrecht, C. M. Nakamura, R. S. Vallery, and D. W. Gidley, Doppler-broadening measurements of positronium thermalization in gases, Phys. Rev. A **67**, 022504 (2003).
[66] F. Saito, Y. Nagashima, and T. Hyodo, Momentum-transfer cross sections for slow positronium-gas collisions, J. Phys. B: At., Mol. Opt. Phys. **36**, 4191 (2003).
[67] Y. Nagashima, T. Hyodo, K. Fujiwara, and A. Ichimura, in *The International Conference on the Physics of Electronic and Atomic Collisions, Vancouver, 1995, Abstracts of Contributed Papers* (1995).
[68] Y. Sano, Y. Kino, T. Oka, and T. Sekine, Kinetic energy of Ps formed by Ore mechanism in Ar gas, J. Phys.: Conf. Ser. **618**, 012010 (2015).
[69] P. A. Fraser, The scattering and pick-off quenching of orthopositronium in helium, J. Phys. B: At. Mol. Phys. **1**, 1006 (1968).
[70] M. I. Barker and B. H. Bransden, The quenching of orthopositronium by helium, J. Phys. B: At. Mol. Phys. **1**, 1109 (1968).
[71] M. I. Barker and B. H. Bransden, The quenching of orthopositronium by helium, J. Phys. B: At. Mol. Phys. **2**, 730 (1969).
[72] R. J. Drachman and S. K. Houston, Simplified model for positronium-helium scattering, J. Phys. B: At. Mol. Phys. **3**, 1657 (1970).
[73] P. K. Biswas and S. K. Adhikari, Scattering of positronium by H, He, Ne, and Ar, Chem. Phys. Lett. **317**, 129 (2000).
[74] H. Saito and T. Hyodo, Experimental Evidence for Spin-Orbit Interactions in Positronium-Xe Collisions, Phys. Rev. Lett. **97**, 253402 (2006).
[75] J. DiRenzi and R. J. Drachman, Re-examination of a simplified model for positronium-helium scattering, J. Phys. B: At., Mol. Opt. Phys. **36**, 2409 (2003).
[76] J. Hofierka, B. Cunningham, C. M. Rawlins, C. H. Patterson, and D. G. Green, Many-body theory of positron binding to polyatomic molecules, Nature (London) **606**, 688 (2022).
[77] J. Mitroy and S. A. Novikov, Spin-Orbit Quenching of Positronium during Atomic Collisions, Phys. Rev. Lett. **90**, 183202 (2003).
[78] D. A. Varshalovich, A. N. Moskalev, and V. K. Khersonskii, *Quantum Theory of Angular Momentum* (World Scientific, Singapore, 1988).
[79] P. G. Burke, *Potential Scattering in Atomic Physics* (Springer, New York, 1977).